Human Molecular Genetics, 2019, Vol. 28, No. 18 3072–3090

doi: 10.1093/hmg/ddz122
Advance Access Publication Date: 7 June 2019
General Article

GENERAL ARTICLE

Mouse models of X-linked juvenile retinoschisis have an early onset phenotype, the severity of which varies with genotype

Yang Liu[1,†], Junzo Kinoshita[2,†,‡], Elena Ivanova[3,†], Duo Sun[1], Hong Li[1], Tara Liao[1], Jingtai Cao[1], Brent A. Bell[2,§], Jacob M. Wang[2], Yajun Tang[1], Susannah Brydges[1], Neal S. Peachey[2,4,5], Botir T. Sagdullaev[3] and Carmelo Romano[1,*]

[1]Regeneron Pharmaceuticals, Tarrytown, NY 10591, USA [2]Cole Eye Institute, Cleveland Clinic, Cleveland, OH 44195, USA [3]Burke Neurological Institute at Weill Cornell Medicine, White Plains, NY 10605, USA [4]Louis Stokes Cleveland VA Medical Center, Cleveland, OH 44106, USA and [5]Department of Ophthalmology, Cleveland Clinic Lerner College of Medicine of Case Western Reserve University, Cleveland, OH 44195, USA

*To whom correspondence should be addressed at: Regeneron Pharmaceuticals, 777 Old Saw Mill River Road, Tarrytown, NY 10591, USA. Tel: +1 9148477122; Fax: +1 9148477393; Email: carmelo.romano@regeneron.com

Abstract

X-linked juvenile retinoschisis (XLRS) is an early-onset inherited condition that affects primarily males and is characterized by cystic lesions of the inner retina, decreased visual acuity and contrast sensitivity and a selective reduction of the electroretinogram (ERG) b-wave. Although XLRS is genetically heterogeneous, all mouse models developed to date involve engineered or spontaneous null mutations. In the present study, we have studied three new *Rs1* mutant mouse models: (1) a knockout with inserted *lacZ* reporter gene; (2) a C59S point mutant substitution and (3) an R141C point mutant substitution. Mice were studied from postnatal day (P15) to 28 weeks by spectral domain optical coherence tomography and ERG. Retinas of P21–22 mice were examined using biochemistry, single cell electrophysiology of retinal ganglion cells (RGCs) and by immunohistochemistry. Each model developed intraretinal schisis and reductions in the ERG that were greater for the b-wave than the a-wave. The phenotype of the C59S mutant appeared less severe than the other mutants by ERG at adult ages. RGC electrophysiology demonstrated elevated activity in the absence of a visual stimulus and reduced signal-to-noise ratios in response to light stimuli. Immunohistochemical analysis documented early abnormalities in all cells of the outer retina. Together, these results provide significant insight into the early events of XLRS pathophysiology, from phenotype differences between disease-causing variants to common mechanistic events that may play critical roles in disease presentation and progression.

[†]The authors wish it to be known that, in their opinion, the first three authors should be regarded as joint first authors.
[‡]Present address: Medicinal Safety Research Laboratories, Daiichi Sankyo Co., Ltd, Tokyo, Japan.
[§]Present address: Scheie Eye Institute, University of Pennsylvania, Philadelphia, PA, USA.

Received: February 11, 2019. **Revised:** May 4, 2019. **Accepted:** June 3, 2019

Introduction

X-linked retinoschisis (XLRS; OMIM: 312700) is a juvenile onset progressive retinal degeneration characterized by cystic retinal lesions and by macular schisis that follows a spoked-wheel pattern (1). Functional impairments in XLRS include decreased visual acuity and loss of contrast sensitivity (2,3), as well as a reduced b-wave of the electroretinogram (ERG), indicative of panretinal involvement (4,5). As an X chromosome-linked trait, XLRS primarily affects males, although females with XLRS have been reported in consanguineous families (6–9). XLRS is caused by mutations in *Retinoschisin 1* (*RS1*) (10), which encodes the 224-amino acid protein retinoschisin (RS1). XLRS is genetically heterogeneous, with disease caused by deletions, insertions, splice site or missense mutations predicted to impact RS1 secretion, octamerization or other function, with a corresponding manifestation in disease severity (11–14).

In the developing mouse retina, *Rs1* is reported to be expressed by multiple retinal cell types (15), suggesting that RS1 is required for multiple aspects of retinal development. As development proceeds, *Rs1* expression becomes restricted to photoreceptors. The protein is secreted as disulfide bond-stabilized homo-octamers, which are transported to other retinal sites (1) as double octamers (16). Four *Rs1* mutant mouse models have been reported, including three knockouts (KO) (17–19). A more recent knock-in model expresses a human disease-causing early stop mutation, and likely also manifests as a null mutation (Y65X) (20). These *Rs1* mutants replicate key features of the human condition, including intraretinal schisis and a reduced ERG b-wave (17–20) and have been important for developing gene replacement therapy for XLRS to the point of a clinical trial (21,22). The advent of clinical gene therapy trials for XLRS underscores the importance of understanding XLRS pathophysiology and raises a series of interconnected questions regarding the significance of early *Rs1* expression. At the tissue level, what is the early phenotype of *Rs1* mouse mutants and what is the impact of the specific mutation? Do XLRS mutations affect the distribution of secreted RS1 protein and is this relevant to the disease phenotype? At the cellular level, does mutant *Rs1* impact the structure of the different cell classes of the outer and inner retina, and how do these changes impact retinal ganglion cell (RGC) output? To address these questions, and to provide experimental systems in which to evaluate potential genetic based therapies, we have created new *Rs1* mouse lines. To model null XLRS mutations, we have engineered an *Rs1* KO with insertion of *LacZ* as a reporter. We have also created two human XLRS missense mutation models: C59S, to represent a secreted, but improperly assembled RS1 and R141C, which causes intracellular retention (1, 23). In each of these models, we documented an early and severe disease phenotype using clinically relevant measures (spectral domain optical coherence tomography [SD-OCT]; ERG), which were nevertheless quantitatively different with respect to disease severity. We also reported marked changes in the structure of virtually all retinal cell types, accompanied by abnormal RGC activity.

Results

RS1 expression is primarily limited to photoreceptors

Replacement of the *Rs1* open reading frame with the *LacZ* coding sequence allows expression of the β-galactosidase enzyme wherever *Rs1* is normally expressed. Tissues can then be stained with the synthetic substrate X-gal, which is converted to a blue reporter product wherever enzymatic activity is present, allowing visualization of the time course and location of *Rs1* expression during development. Figure 1A–F compares X-gal staining at key developmental time points. In the KO retina, only a small number of X-gal positive cells were seen in the ganglion cell layer (GCL) at early ages (see inserts to Fig. 1A and B). By P14 (Fig. 1C), strong X-gal staining was seen in the photoreceptor layer and this restricted localization is maintained at later ages (Fig. 1D and E). In contrast, in wild-type (WT) mice, only slight blue coloration was observed in the inner segments, likely reflecting non-specific labeling (Fig. 1F). Only a small fraction of RGCs were labeled, minimally, by X-gal (Fig. 1A and B) and X-gal positive cells were not seen outside of the outer nuclear layer (ONL).

We also examined *Rs1* expression using *in situ* hybridization with RNAScope®. *Rs1* mRNA expression via RNAScope® demonstrated endogenous *Rs1* mRNA expression in WT animals (Fig. 1G–K). *Rs1* mRNA was not detected in retinas from *Rs1* KO animals (Fig. 1L). In WT, *Rs1* mRNA was not detected at P1 (Fig. 1G) and appeared around P7 (Fig. 1H), increasing at later ages with an expression that was restricted to photoreceptors (Fig. 1J and K). It appears that the degree of *Rs1* expression outside of photoreceptors we observed is substantially lower than noted previously (15).

RS1 is a secreted protein (1). To examine how the human XLRS point mutations impact protein distribution, we used an antibody against RS1. In WT mice, RS1 is seen throughout the retina (Fig. 2A), with prominent labeling seen in the photoreceptor inner segments. There are clear synaptic associations in both the outer plexiform layer (OPL) and inner plexiform layer (IPL), but we are not describing this in detail here. RS1 label is also present in both ONL and INL, where it is located in, or on, processes. The methods employed do not permit a discrimination between intracellular and extracellular location of the RS1 protein. This panretinal distribution is nevertheless consistent with prior reports (1), and the specificity of the RS1 antibody is supported by the absence of RS1 labeling in the KO retina (Fig. 2B). Non-specific staining of blood vessels is seen in the KO (Fig. 2B) and point mutant strains due to the secondary antibody, which is an anti-mouse binding to endogenous mouse IgG. In both the C59S (Fig. 2C) and R141C (Fig. 2D) mutants, RS1 staining is restricted to the photoreceptor inner segments, presumably the site of synthesis of the mutant protein.

RS1 protein levels are decreased in Rs1 mutant retina

To examine the impact of the *Rs1* mutations on total RS1 expression, we examined adult retinas by western blot and ELISA. Western blot under reducing condition was used to compare RS1 expression in WT and *Rs1* mutant mouse retinas. RS1 expression was not detected in the KO retina (Fig. 2E) and, in comparison to WT, was dramatically reduced in both C59S (Fig. 2F) and R141C (Fig. 2G) mouse retinas. This low level of RS1 was confirmed by ELISA, where RS1 protein levels were reduced to approximately 15% and 11% of WT in the C59S and R141C retinas, respectively (Fig. 2H). The amount and distribution of mutant RS1 in the adult retina is clearly different from that seen in WT, but the presence of these aberrant forms could impact the disease phenotype. To examine this possibility, we examined structural and functional properties of the *Rs1* mutant retinas.

Rs1 mutant disease phenotype is genotype dependent

We used SD-OCT and ERG to compare the phenotypes of the different *Rs1* mutant lines and how these change with age. Different

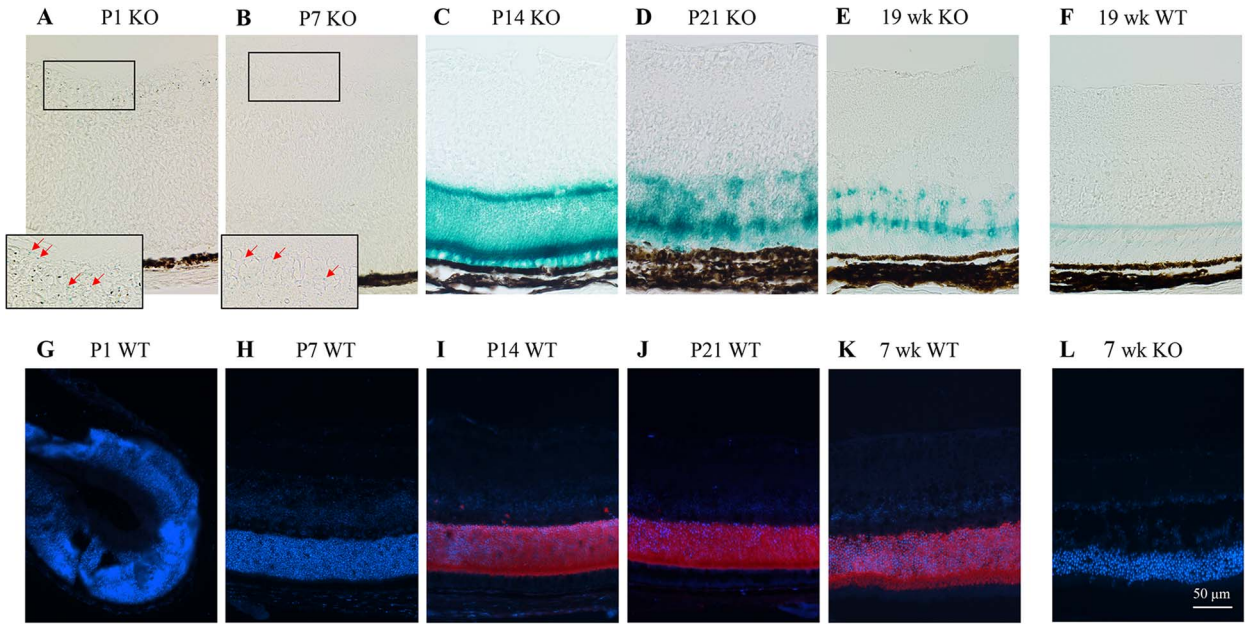

Figure 1. Localization of RS1 in the developing retina. (**A–E**) *Rs1* KO retinas stained for X-gal at the ages indicated. Red arrows in the insets to (A and B) indicate some of the small number of RGCs that were X-gal positive. After P14, X-gal staining was restricted to the photoreceptors (**C–E**). (**F**) WT retina stained for X-gal demonstrates the level of background label in the OPL and inner segments. (**G–K**) RNAScope® showed *Rs1* mRNA in WT mice at the ages indicated. *Rs1* was not detected at P1 (G) or P7 (H). At later ages, *Rs1* was seen in a small number of cells outside of the ONL at P14 (I) and was restricted to photoreceptors at P21 (J) or adulthood (K). Retinal expression of *Rs1* was not detected in the *Rs1* KO retina (**L**).

cohorts of animals were examined at P15, P18, P21 and P24 by SD-OCT imaging and ERG. Adult mice were examined by both techniques, allowing 3–4 days in between test sessions. Figure 3 presents SD-OCT images of the temporal retina for representative WT and *Rs1* mutant mice at each of the ages studied. Retinal schisis is absent in WT littermates but is prominent in each of the *Rs1* mouse lines (see arrowheads), until the later adult ages when schisis becomes less apparent. To compare across age and genotype, we developed three measures, which are diagrammed in Figure 4. To quantify the magnitude of schisis, we measured the area of the INL + OPL in pixels (Fig. 4A, top). Severe schisis was present at the earliest age examined (P15) in all *Rs1* mutant lines, and then receded in older animals, reaching a stable level at P24, which is retained in adult mice (Fig. 4B, top). Schisis severity peaked at P15 for the KO and at P18 for the C59S and R141C point mutants, declining after these peaks at later ages. The later peak seen in the two *Rs1* point mutants indicates that the presence of mutant RS1 might be of some benefit for the developing *Rs1* mutant retina. Photoreceptor involvement has been documented in XLRS patients (24,25) and prior *Rs1* KO mouse models (17–20). We measured the thickness of the outer retina in microns (Fig. 4A, middle). Outer retinal thickness was already reduced at P15 in each of the *Rs1* mutant retinas and thereafter declined, reaching a stable level by P24 (Fig. 4B). Results of the three *Rs1* mutants largely overlapped at all ages. We measured overall retinal thickness at three retinal locations (Fig. 4A, bottom). This measure was elevated in all three *Rs1* mutants at the young ages from P15 to P21 (Fig. 4B, bottom), reflecting the impact of schisis on overall retinal thickness. At P24 and in adult mice, overall retinal thickness measures were similar in the *Rs1* mutants and WT mice, reflecting the counterbalancing effects of schisis, which increases overall retinal thickness, and outer retinal thinning, which decreases overall retinal thickness.

Prior to the discovery of the *Rs1* gene and the ability to observe retinal schisis *in vivo* using SD-OCT imaging, a reduced b-wave on ERG testing was a critical component of XLRS diagnosis. In studies of human XLRS patients, the extent of ERG involvement has also been shown to discriminate XLRS subtypes based on the nature of the underlying *RS1* mutation (14). To compare the disease phenotypes of three *Rs1* mutant mouse lines, and determine how these change with age, we recorded ERGs under dark- and light-adapted conditions from mice at early ages (P15, P18, P21 and P24), where severe schisis was observed on SD-OCT imaging, and also at adult ages (12–28 weeks). Figure 5 presents a series of dark-adapted ERGs obtained from representative mice at P15 (Fig. 5A), P24 (Fig. 5B) and at 10 weeks of age (Fig. 5C). From the earliest time point, the ERG was reduced in amplitude in each of the *Rs1* mutants as compared to WT. The a-wave reduction was consistent with the thinned ONL observed on SD-OCT imaging. In each *Rs1* mutant, the b-wave component was reduced more than the a-wave, indicating that these mouse models replicate another main feature of the human XLRS phenotype, a 'negative ERG' waveform. Negative ERGs were seen at every age examined in all three *Rs1* mutants. Of the three *Rs1* mutants, the KO showed the greatest ERG b-wave reduction at P15 and P24, while the b-waves of C59S and R141C mice were comparable (Fig. 5A, B, D, E). This less severe phenotype also suggests that the presence of mutant C59S or R141C RS1 provides some benefit to the function of the developing retina. At adult ages, however, ERGs of C59S mice were larger than those of either KO or R141C animals (Fig. 5C and F).

Figure 6 presents a series of light-adapted cone ERGs obtained from representative mice at P15 (A), P24 (B) and at 10 weeks of age (C). The cone ERG was reduced in amplitude in each of the *Rs1* mutants as compared to WT at all ages examined (Fig. 6D–F). Of the three *Rs1* mutants, the cone ERG b-waves of KO mice were smallest at early ages, while responses

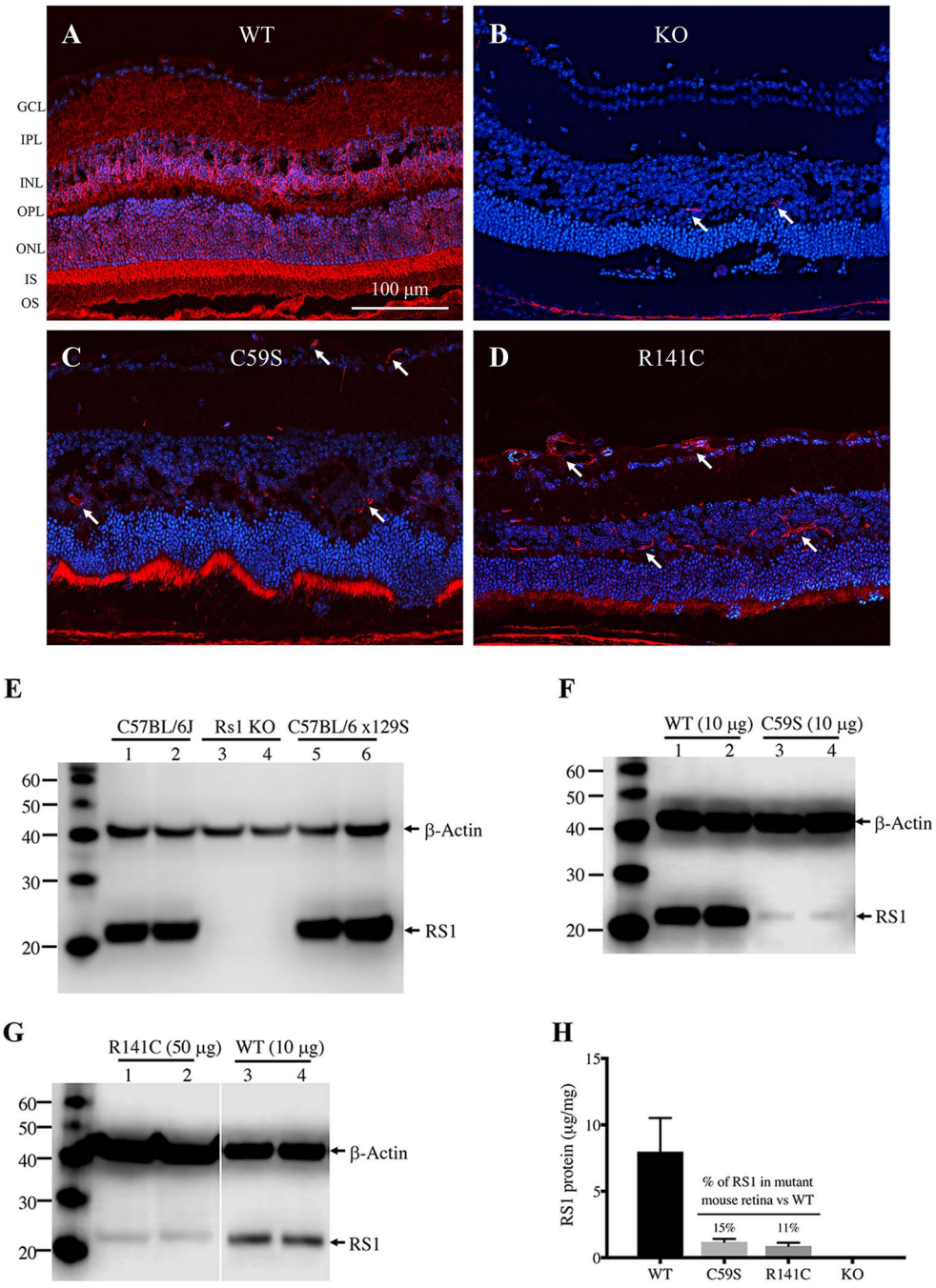

Figure 2. Immunohistochemical localization of RS1 (red) in adult WT (**A**), KO (**B**), C59S (**C**) and R141C (**D**) retinal cross-sections. In the WT, RS1 is present in all retinal layers (A). This distribution is missing in the KO retina (B) and is restricted to the inner segments of C59S (C) and R141C (D) retina. Non-specific labeling of blood vessels (red arrows) is seen, due to the use of an anti-mouse secondary antibody. Scale bar indicates 100 µm in (A). Western blot analysis of Rs1 in KO (**E**), C59S (**F**) and R141C (**G**) retina. (**H**) ELISA-based quantification of RS1 demonstrated significant reduction in each mutant. Bars indicate average (±SD) for four retinas.

of C59S and R141C mice were comparable (Fig. 6A, B, D, E). At adult ages, however, ERGs of C59S mice were substantially larger than those of either KO or R141C animals (Fig. 6C and F). The cone ERG results mirror those obtained under dark-adapted conditions (Fig. 5) and strengthen the conclusion that disease severity varies with genotype in these models.

To evaluate the age-related changes, we derived amplitude parameters for the dark-adapted a-wave using the Lamb & Pugh model of rod phototransduction (26) and for the ERG b-wave using the Naka–Rushton equation (27). These fits are summarized in Figure 7 for R_{mP3} and A fit to the leading edge of the dark-adapted ERG a-wave (Fig. 7A and B), for R_{max} and K fit to the initial limb of the dark-adapted ERG b-wave luminance-response function (Fig. 7C and D) and for R_{max} and K fit to the cone ERG luminance-response function (Fig. 7E and F). In WT mice, the a-wave amplitude parameter R_{mP3} increased in amplitude between P15 and P24, and then maintained a stable level in adulthood (Fig. 7A). R_{mP3} values of KO mice were consistently reduced in

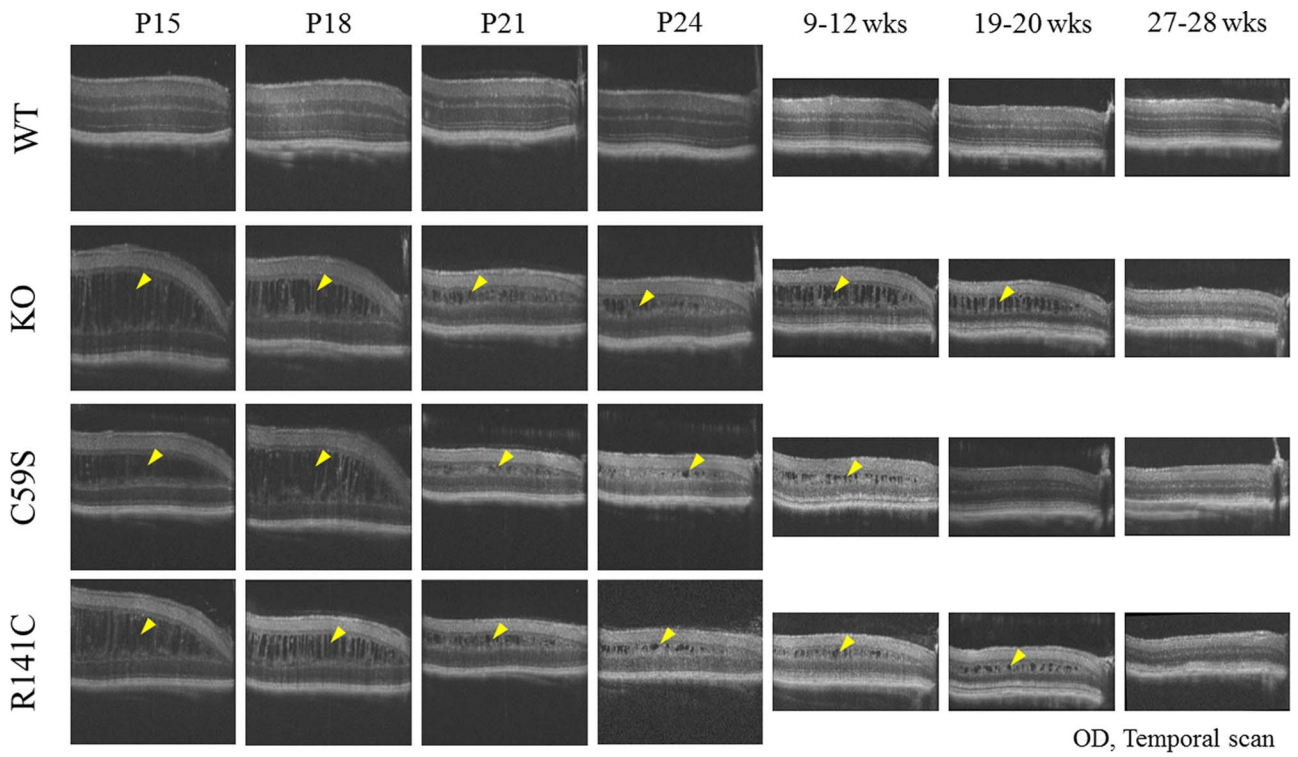

Figure 3. Representative SD-OCT images of the retina in WT, KO, C59S and R141C mice at the ages indicated. All images were obtained from the temporal region of the right eye, and include the edge of the ONH on the right. Yellow arrowheads indicate schisis.

comparison to WT, throughout the age range examined. R_{mP3} values of C59S and R141C mice were reduced at all ages except for the earliest age examined—P15. In adult mice, the reduction was significant in C59S mice, but less severe as compared to the KO or R141C mutant lines (Fig. 7A). In comparison to WT values, the phototransduction gain parameter A was consistently reduced between P15 and P24 in all three *Rs1* models (Fig. 7B). In adults, we noted a divergence between *Rs1* genotypes, so that A values were elevated in C59S, unchanged in R141C and decreased in KO mice.

In WT mice, values of the ERG b-wave amplitude parameter R_{max} increased from P15 to P24 and then maintained a steady level in adulthood, for both dark-adapted (Fig. 7C) and light-adapted (Fig. 7E) responses. R_{max} values were markedly reduced in all *Rs1* mutant lines, from the earliest age examined. R_{max} values overlapped across all three genotypes from P15 to P21. In adult mice, R_{max} values of C59S mice were consistently larger than those of KO or R141C animals (Fig. 7C and E). For the dark-adapted ERG, values of the semi-saturation constant *K* were consistently elevated in *Rs1* mutants as compared to WT, indicating that more light was required to evoke a response equal to half of R_{max} (Fig. 7D). For the light-adapted ERG, *K* values were often elevated in *Rs1* mutants as compared to WT (Fig. 7F), but at P21 and P24 were actually lower than see in WT, perhaps indicating a decreased response to the background field.

For the C59S and R141C lines, photoreceptors of female heterozygotes express a mutant or WT allele in different cells due to X inactivation. Although human *RS1* heterozygotes are generally thought of as carriers without a clinical phenotype, visual abnormalities have been reported in some of these individuals (28–30) attributable to random X inactivation impacting a large fraction of WT alleles in a given retinal area. Our observation that both C59S and R141C mutant proteins are detectable in the retina (Fig. 2), coupled with the current model in which RS1 interacts extracellularly to develop the functional double octamer (16), raises the possibility that female C59S/+ or R141C/+ heterozygotes might have a phenotype. To examine this, for each *Rs1* mutant line we compared results of 10- to 11-week-old female mice that were either homozygous WT (+/+), *Rs1* mutant homozygotes (*m/m*) or *Rs1* mutant heterozygotes (*m*/+). When we examined these mice by SD-OCT, we noted no schisis in *m*/+ heterozygotes for any line, which instead appeared comparable to homozygous WT littermates (Supplementary Material, Fig. S1). In comparison, schisis was clearly present in the retinas of *m/m* females (Supplementary Material, Fig. S1). A similar conclusion was reached from ERG analysis, where the response functions of +/+ and *m*/+ female mice were in close agreement, while those of homozygous *m/m* females mirrored those of *Rs1* mutant male littermates for both dark-adapted (Supplementary Material, Fig. S2) and light-adapted (Supplementary Material, Fig. S3) stimulus conditions. The RS1 content of the heterozygous KO females was comparable to that seen in homozygous WT females and WT male hemizygotes (Supplementary Material, Fig. S4).

Altered patterns of spontaneous activity in Rs1 mutant mice

The above results establish that each *Rs1* mutant mouse model presents a disease phenotype that recapitulates key features of human XLRS. To better understand the XLRS phenotype and to determine the role of RS1 in retinal signaling and how it may differ across various *Rs1* mutants, we evaluated baseline and light-evoked activity of RGCs. For this study, we focused on early ages (P19–P22), which correspond to the rapid phase of disease progression. Electrophysiological assessment was then followed

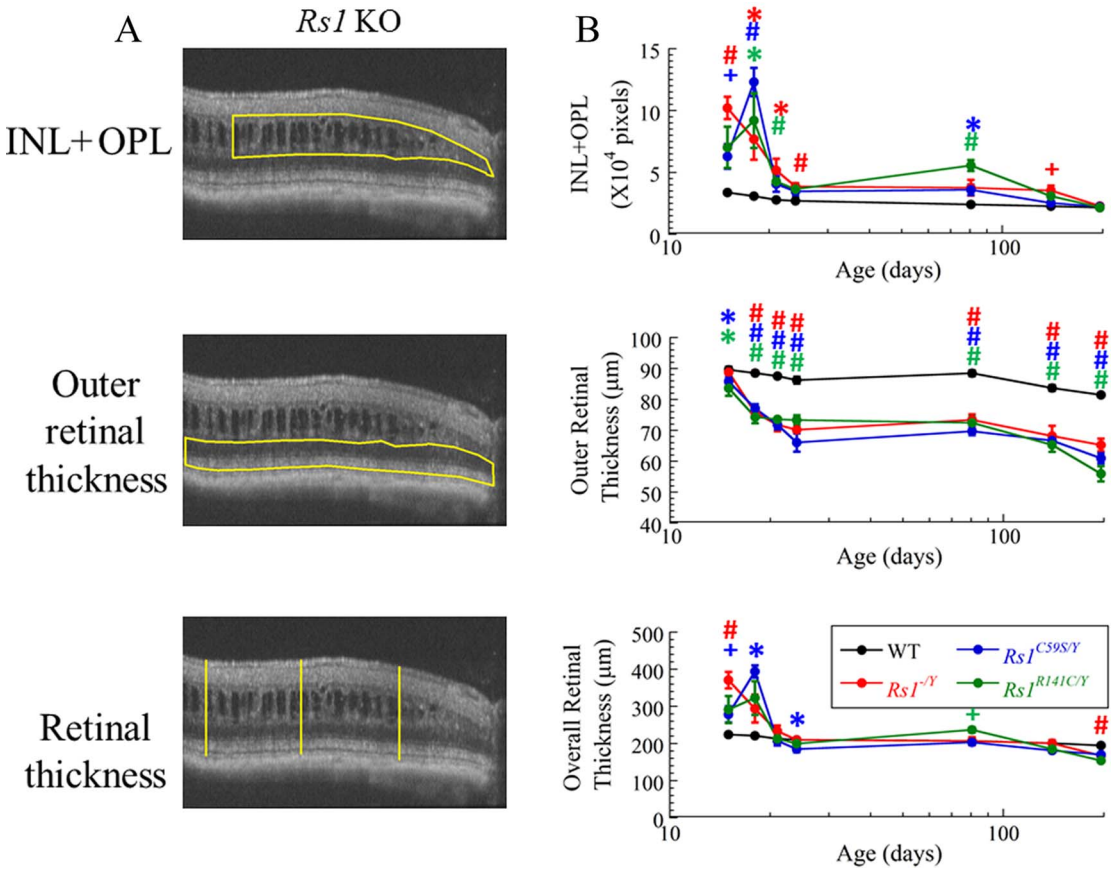

Figure 4. Quantitation of retinal parameters used to compare WT and *Rs1* mutant retinas. (**A**) Diagram of method to measure INL + OPL area (top), the thickness of the outer retina (middle) and the thickness of the overall retina (bottom). This image was obtained from the right temporal retina of a 20-week-old KO mouse. (**B**) Measures plotted as a function of age for each of the mouse lines examined. Data points indicate average (±SEM) for 3–16 mice. Symbols above the data points at each age indicate the results of *t*-tests comparing *Rs1* values to those of WT. ∗ indicates $P < 0.05$; + indicates $P < 0.01$; # indicates $P < 0.001$ and the color indicates which *Rs1* model is being compared to WT.

by a structural analysis of the major cellular components in KO, C59S and R141C mice.

RGCs are the output retinal neurons that integrate the retinal activity along distinct parallel visual channels (31). First, we compared the resting spontaneous activity of identified ON- and OFF-type RGCs (Fig. 8A and C), the two major visual pathways responsible for detecting light increments and decrements. ON and OFF retinal pathways are established at the synapse between photoreceptors and ON (depolarizing) or OFF (hyperpolarizing) bipolar cells (BCs), a primary site of *Rs1* pathology (32).

For patch-clamp recordings, spiking activity was characterized for RGCs that responded to a test spot of light, thus contributing to visual signaling. As shown in the raster plots from these light responsive RGCs, there was a significant increase in spontaneous firing rate in *Rs1* mutant mice, compared to WT controls, in both ON and OFF RGCs (Fig. 8B, D, E, F), suggesting similar changes in both ON and OFF presynaptic BC circuits (further tested and confirmed by the immunohistochemical analysis shown in Fig. 10). This elevation was significant for KO and C59S RGCs, but not for RGCs of R141C mice. We attribute the R141C results to a wider cell-to-cell variability of activity patterns seen in this *Rs1* mutant. While some R141C RGCs were hyperactive, we also encountered a large number of quiescent cells that did not respond to light. In all *Rs1* mutants, we encountered swollen and fragile cells that could not be targeted for single-cell recording due to inability to establish electrical contact. No such cells were observed in WT retinas. In WT mice ($n = 12$), we recorded a total of 33 RGCs, each of which was responsive to light and exhibited low-to-moderate spontaneous activity, with firing rates ranging from 0.5 to 7.5 action potentials per second (AP/s) (mean 3.05 ± 0.38 AP/s). In KO mice ($n = 10$), 24/31 RGCs responded to light and these had an elevated spontaneous firing rate (range 1–30 AP/s, mean 10.46 ± 1.48 AP/s). In C59S mice ($n = 8$), 24/33 RGCs responded to light and had an elevated spontaneous firing rate (range 1–18 AP/s, mean 9.36 ± 0.99 AP/s). In comparison, in R141C mice ($n = 6$), only 15 out of 39 RGCs responded to light and exhibited elevated spontaneous activity (range 2–18 AP/s, mean 8.20 ± 1.51 AP/s).

RGCs of Rs1 mutants have disrupted detection of visual stimuli

The elevated spontaneous activity seen in *Rs1* mutant RGCs has important implications for visual processing and the ability to detect stimuli. To determine how the elevated spontaneous activity observed in *Rs1* mutants impacts visual detection, we examined RGC responses to spot stimuli that matched the RGC receptive field center. The contrast of the spot was matched to the sign of the RGC center (increment for ON RGCs and decrement for OFF RGCs) and was increased in 0.5 log steps to obtain an intensity-response function. From this response series, we determined the visual stimulus producing the largest change in

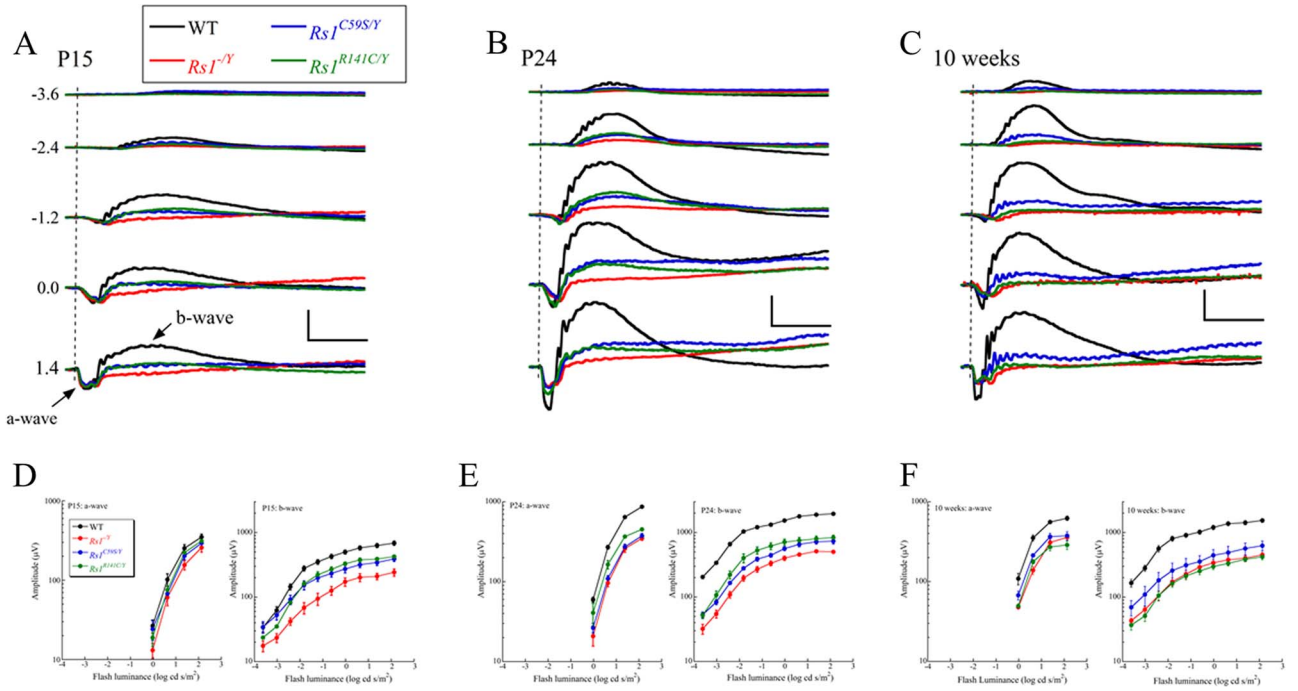

Figure 5. Dark-adapted electroretinography. Representative dark-adapted ERGs obtained from mice aged P15 (**A**), P24 (**B**) or 10 weeks (**C**). Note that responses of *Rs1* mutant mice are reduced at all ages and display the characteristic negative ERG waveform. Scale bars indicate 500 μV and 100 ms. Luminance-response functions for the major ERG components compare data from mice aged P15 (**D**), P24 (**E**) or 10 weeks (**F**). Data points indicate the average (±SEM) for 3–16 mice.

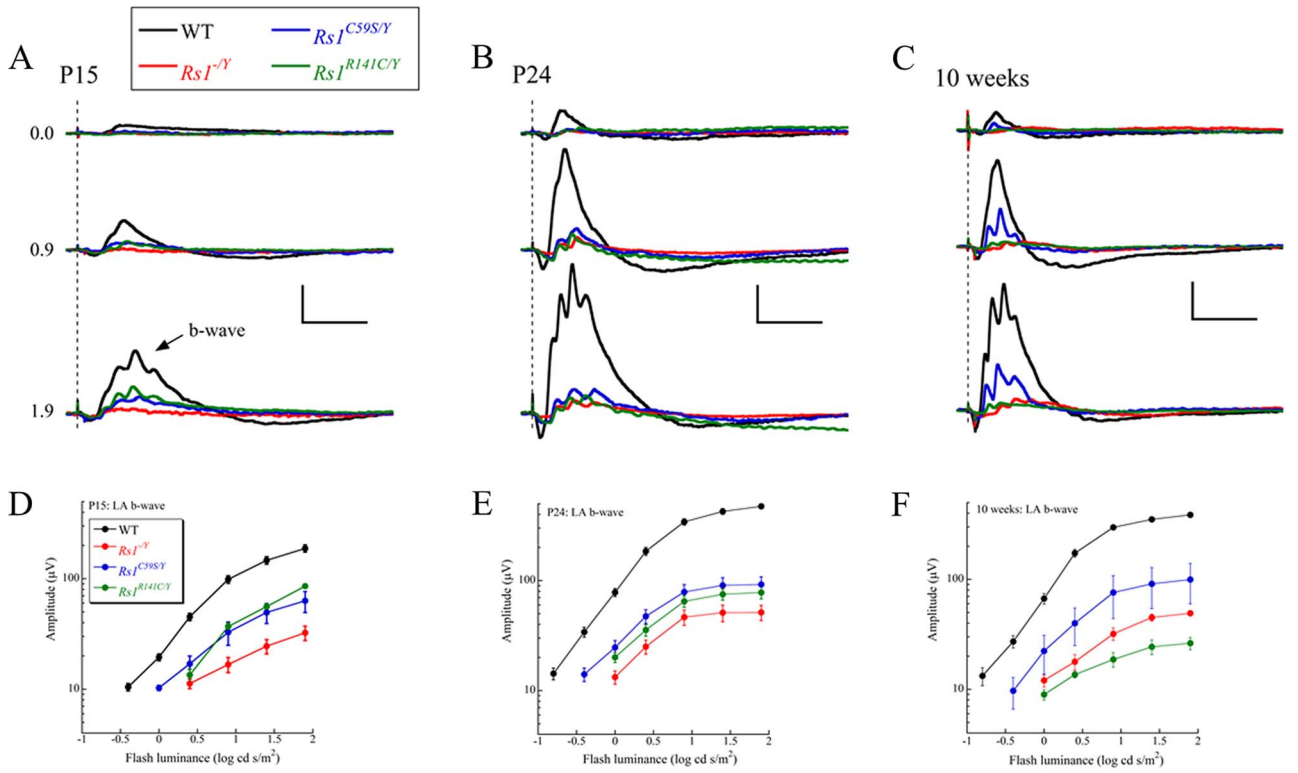

Figure 6. Light-adapted electroretinography. Representative light-adapted cone ERGs obtained from mice aged P15 (**A**), P24 (**B**) or 10 weeks (**C**). Note that responses of *Rs1* mutant mice are reduced at all ages. Scale bars indicate 100 μV and 100 ms. Luminance-response functions for the cone ERG from mice aged P15 (**D**), P24 (**E**) or 10 weeks (**F**). Data points indicate the average (±SEM) for 3–16 mice.

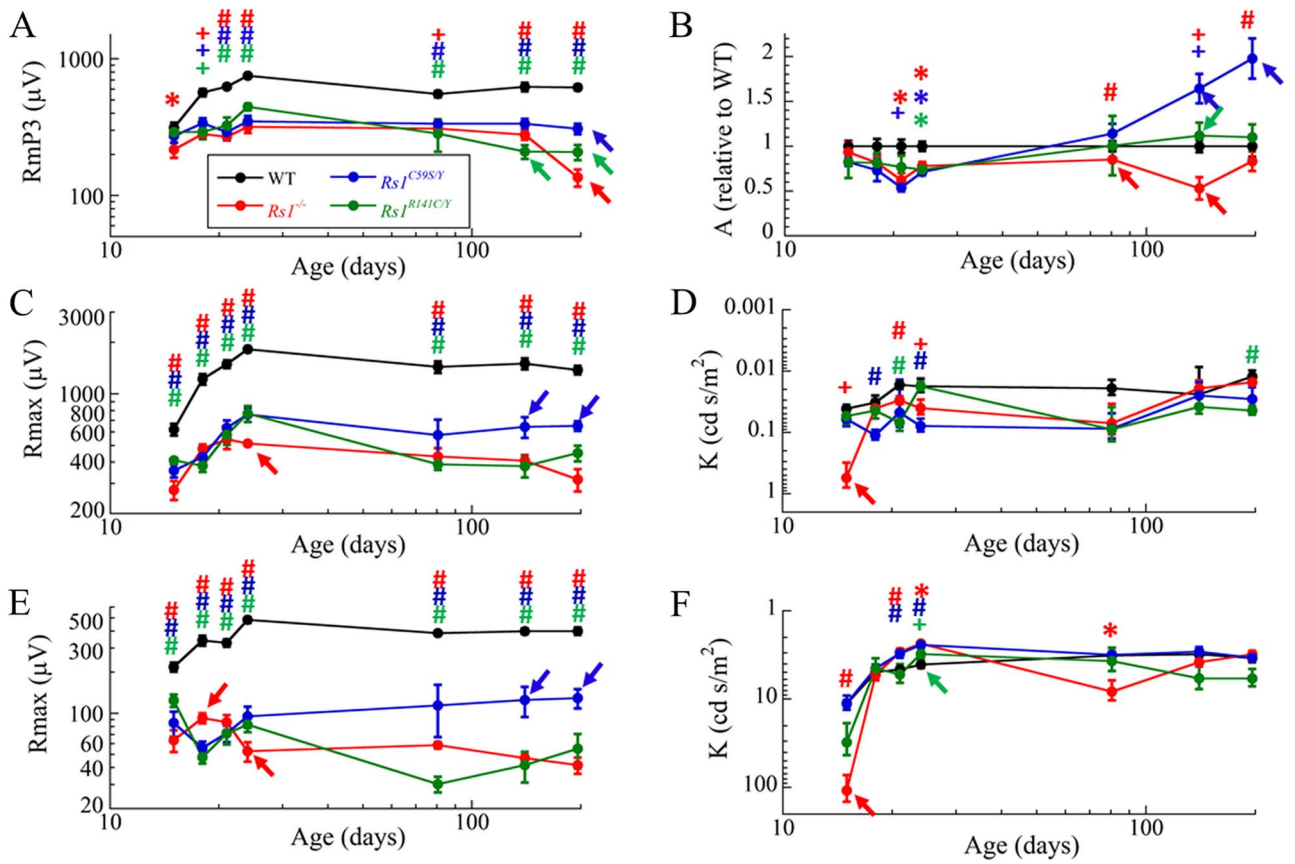

Figure 7. Age-related changes in ERG amplitude parameters. R_{mP3} (**A**) and *A* (**B**) parameters obtained by fitting the Lamb & Pugh equation to the leading edge of the dark-adapted ERG a-wave. R_{max} (**C**) and *K* (**D**) parameters obtained by plotting the Naka–Rushton equation to the initial limb of the dark-adapted b-wave response function. R_{max} (**E**) and *K* (**F**) parameters obtained by plotting the Naka–Rushton equation to the light-adapted b-wave response function. Data points indicate the average (±) SEM for 3–16 mice. Symbols above the data points at each age indicate the results of *t*-tests comparing *Rs1* values to those of WT. ∗ indicates $P < 0.05$; + indicates $P < 0.01$; # indicates $P < 0.001$ and the color indicates which *Rs1* model is being compared to WT. Filled arrows indicate where values for one *Rs1* mutant are significantly different from both of the other mutants; the color of the arrow identifies that mutant.

spiking activity, obtained by adjusting the total number of spikes during the light stimulation to the baseline spontaneous activity. In WT ON and OFF RGCs, increasing stimulus strength was paralleled by an increased firing rate (Fig. 9A and C). In comparison, in all *Rs1* mutants, the strongest response was observed at low and moderate stimulus intensities and responses were often suppressed for high-intensity stimuli. This atypical intensity–response relationship is intriguing and suggests disrupted cone photoreceptor activation/adaptation and/or altered photoreceptor signaling to their downstream targets, a topic we return to in relation to our immunohistochemical results.

To determine how elevated RGC activity impacts light detection, we compared signal-to-noise ratios (SNRs) of WT and *Rs1* mutant RGCs. In all *Rs1* mutants, SNR values were decreased significantly as compared to WT (Fig. 9E). Major factors causing this decline were the elevated spontaneous activity (Fig. 8F) and a decreased visual response (Fig. 9D). These findings are consistent with the hypothesis that the elevated activity acts as a barrier for visual signal discrimination. For R141C mutants, however, the SNR deficit was exacerbated further by the decreased visual response, indicating that different *Rs1* mutations induce distinct pathophysiological changes.

Next, to assess whether the aberrant RGC activity was due to presynaptic changes or altered intrinsic RGC activity, we recorded their synaptic inputs and compared them to spiking output. As evident from Figure 9F, both excitatory and inhibitory inputs showed aberrant activity. While further studies will be needed to determine the precise origins of the aberrant activity in *Rs1* mutants, these findings indicate that the visual deficits originate presynaptically and may not reflect an intrinsic RGC pathophysiology.

Cellular changes

ERGs of XLRS patients (4,5) and *Rs1* mutant mice (17–20) are characterized by a greater reduction of the b-wave than the a-wave, although both can be affected. This localizes defects to the outer retina, including abnormal transmission between photoreceptors that generate the a-wave (33) and depolarizing BCs that generate the b-wave component (34,35). Indeed, prior studies have identified abnormalities at the photoreceptor-to-BC synapse (32). The *Rs1* mice studied here share these ERG abnormalities (Figs. 5 and 6) and also display ONL thinning (Figs. 3 and 4) leading us to examine the outer retina at the cellular level. To accomplish this, we used immunohistochemistry to label specific classes of cells. To examine the cone pathway, we labeled cone photoreceptors with cone arrestin (36) and type 6 ON and Type 2 OFF cone BCs with synaptotagmin II (37). Cone arrestin plays a critical role in cone photoreceptor deactivation and adaptation to light (38). Under light-adapted

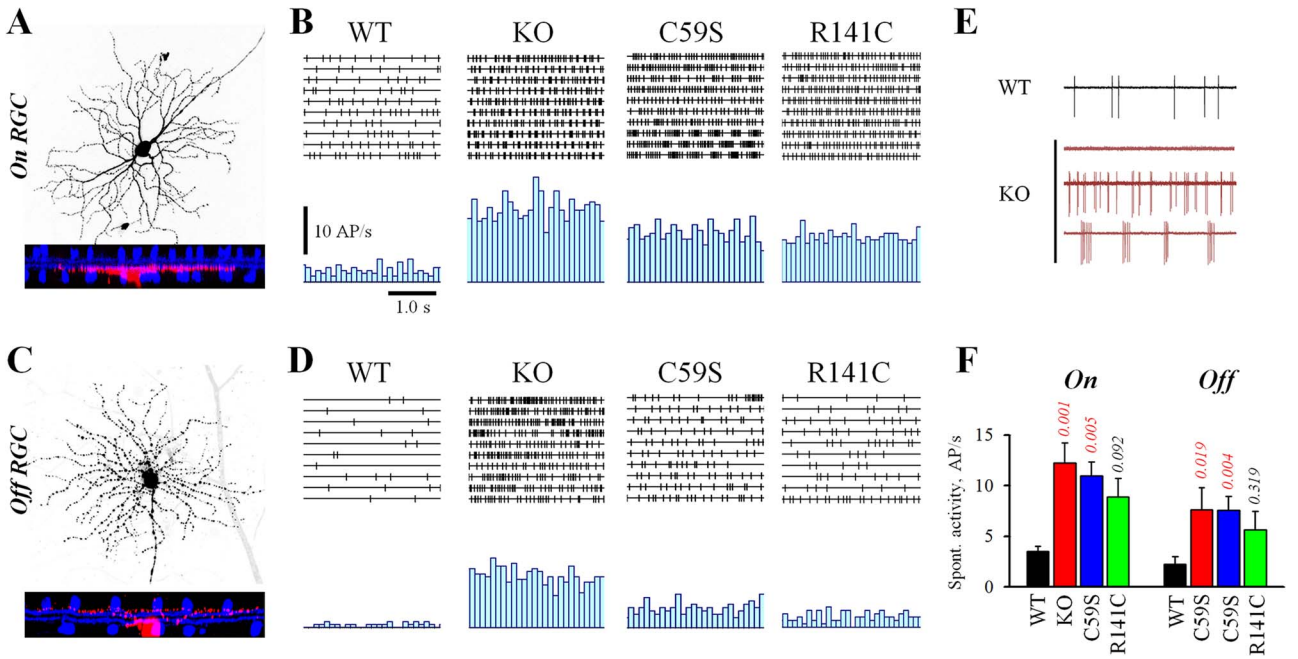

Figure 8. Altered patterns of spontaneous activity in *Rs1* mutant mice. (**A, C**) Confocal reconstructions of representative RGCs following electrophysiological assessment showing distinction between ON and OFF RGC types. Raster plots and peristimulus time histograms show spontaneous activity in ON (**B**) and OFF (**D**) RGCs that were recorded in cell-attached mode at P19–P21 in WT and age-matched *Rs1* mutant male mice. (**E**) Representative traces from a WT and three KO RGCs illustrate a range of activity patterns encountered in the mutants. (**F**) Quantification of spontaneous activity of ON and OFF RGCs in WT and *Rs1* mutant mice. Numbers above each graph bar indicate *P*-values of one-way ANOVA pairwise multiple comparison (Tukey test) of each mutant to the WT RGCs. Each group contains $n = 6–8$ mice with 2–4 RGC of each class per animal. Error bars indicate ±SEM, AP/s—action potentials per second.

conditions, arrestin is primarily localized to cone outer segments (OS) of WT mice, with relatively low levels seen at the synapse (Fig. 10C) (36). In the *Rs1* mutants, arrestin is mislocalized with higher levels seen throughout the cone soma and much higher levels observed at the axon terminal (Fig. 10A and C). KO mice exhibited a reduction of cone arrestin at the OS and an increase at the pedicle. In the C59S retina, the reduction seen in the OS was higher than in the KO, while the elevation in cone pedicles was comparable to KO. In the R141C retina, a strong reduction in cone arrestin was observed in the OS and the elevation at the cone pedicle was greater than any of the other models. The lower density of arrestin in the OS of *Rs1* mutant mice might prolong the recovery time of cones, leading to the diminished responses seen when stronger light stimuli were used in our patch-clamp recordings (Fig. 9A and B). Arrestin labeling also allowed us to examine overall cone structure. In each of the *Rs1* mutants, cone OSs were shortened (Fig. 10A and B [OS]) and the cone pedicles were malformed (Fig. 10A and B [OPL]).

In WT retina, type 6 ON and type 2 OFF cone BCs are labeled for synaptotagmin II (magenta) and make invaginating and flat synapses with cone pedicles, respectively (Fig. 10A and B [OPL]). In *Rs1* mutants, most BC dendrites retained contact with the malformed cone pedicles, suggesting retention of glutamate release from these cone terminals. Numerous dendritic processes of synaptotagmin II-positive BCs nevertheless invaded the ONL in the *Rs1* mutant retinas (Fig. 10A and B [ONL]). We quantified this aberrant sprouting in two ways. First, we determined how far the processes extended into the ONL, by measuring the depth of the ONL reached by 90% of the sprouts (Fig. 10D and F). Second, we measured the total length of processes within a $50 \times 50\ \mu m^2$ segment. To control for differences in ONL thickness among *Rs1* mutants, we measured the length as a percentage of ONL thickness (Fig. 10E and G). ONL sprouting of cone BCs was seen in all three *Rs1* mutants, with the strongest sprouting seen in the KO model (Fig. 10A, F, G). Similar ectopic sprouting from BCs has been observed in another *Rs1* KO mouse model (39), and also in several mouse models involving proteins that control glutamate release from photoreceptor terminals (40–42). This disruption of the photoreceptor-BC interface is likely to contribute to the reduced cone ERG amplitude seen in *Rs1* mutants, as the cone ERG relies on effective transmission from cones to BCs (35). ONL sprouting of cone BCs was seen in all three *Rs1* mutants, with the strongest seen in the KO model (Fig. 10F and G). Cone BC projections into the INL were observed in the KO, and were less prominent in the point mutants (Fig. 10A and B [INL]).

Turning to the rod pathway, aberrant sprouting was also detected in rod BCs (Fig. 11, magenta), and PKC-positive rod BC dendrites were seen to extend toward and into the ONL in all three *Rs1* mutants (Fig. 11A and B [ONL]). Similar to what was observed in cone BCs, sprouting was greater in the KO as compared to the C59S and R141C point mutants. Calbindin-positive horizontal cells (HCs; Fig. 11, green) were also observed to extend their neurites into the ONL (Fig. 11A and B [ONL]), as compared to their normal termination in the OPL of WT mice. HC processes were found close to the sprouting RB dendrites, and they often terminated at the same location in the ONL (Fig. 11B [ONL]). HC sprouting was most prominent in the KO as compared to the C59S and R141C point mutants. Overall, the extent and terminal location of sprouting was similar for CBs, RBs and HCs within each of the mutant lines, suggesting that these processes were attracted to a common source of glutamate release.

Retinal degeneration is normally accompanied by hypertrophy and reactive gliosis of Müller glial cells (43,44). Notably, Müller cell reactive gliosis has been observed in another *Rs1* KO

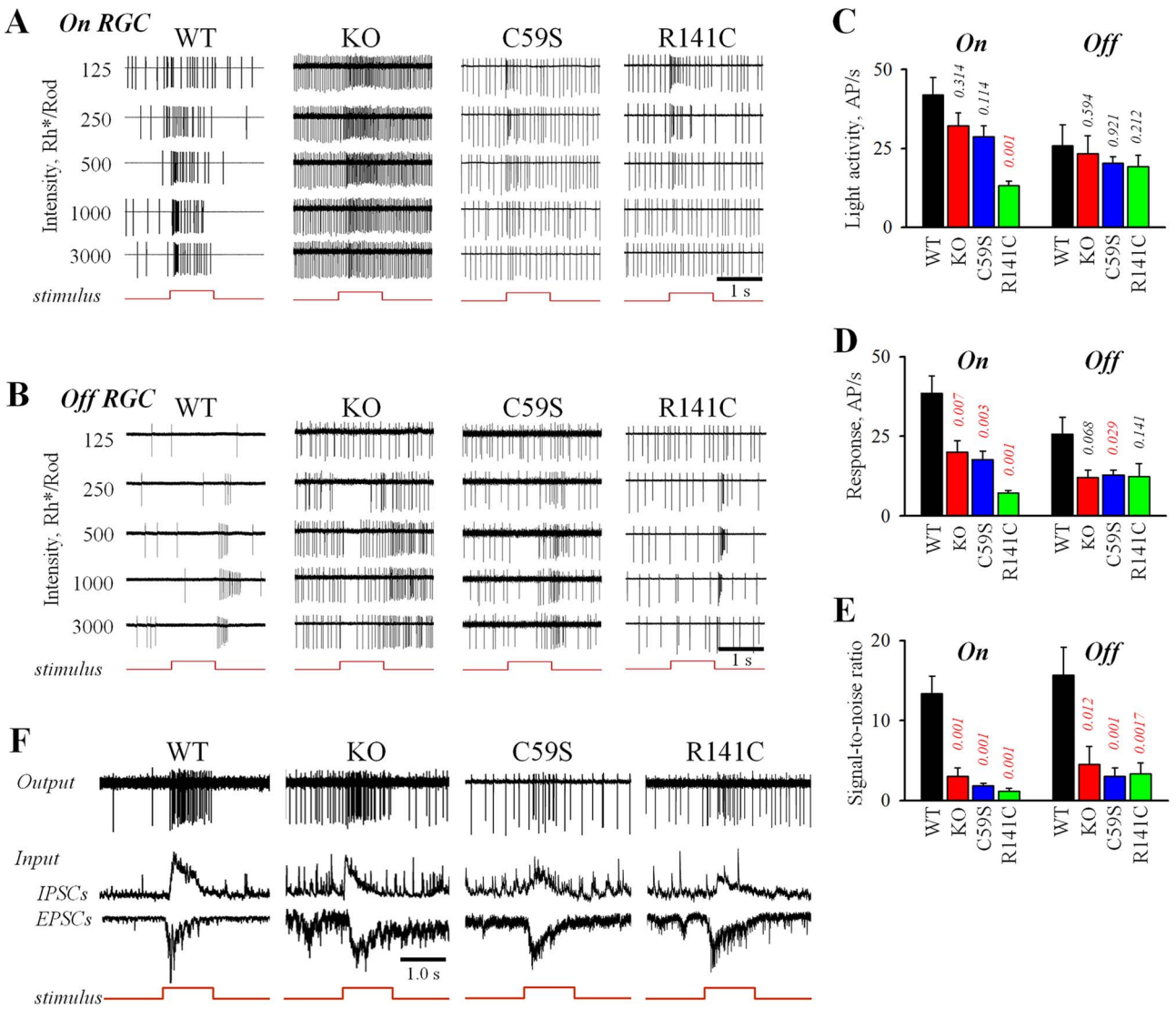

Figure 9. Aberrant activity impairs responses to light in *Rs1* mutant mice. (**A, B**) Series of spiking responses were obtained to a 200 µm spot of light with increasing positive contrast in ON (A) and negative contrast in OFF (B) RGCs. Red steps below activity traces indicate stimulus timing. (**C**) Average spiking activity during light stimulus and the response amplitude, adjusted to spontaneous activity (**D**) in P19–P21 WT and *Rs1* mutant male mice. (**E**) In the recordings from RGCs, elevated spontaneous activity reduces SNR (see Materials and Methods for computation) of retinal output, diminishing discrimination of responses to visual stimulus. Numbers above each graph bar represent *P*-values of one-way ANOVA pairwise multiple comparison (Tukey test) to the WT RGCs. Each group contains $n = 6–8$ mice with 2–4 RGC of each class per animal. Error bars indicate ±SEM, AP/s—action potentials per second. (**F**) Whole-cell recording of excitatory and inhibitory currents underlying spontaneous and light-evoked activities in RGCs in WT and *Rs1* mutant mice.

(39). In WT retina, GFAP labeled only astrocytes (Fig. 11A and B [GCL]). In the *Rs1* mutants, the density of astrocyte processes was significantly higher, which may reflect either increased numbers or activation of these cells. In addition to astrocytes, activated Müller cell processes were seen in all three *Rs1* mutants, and these processes are most readily seen across the ONL (Fig. 11B [ONL]).

Discussion

In this study, we have defined the XLRS phenotype of three new *Rs1* mutant mouse models and then examined several novel features of the disease phenotype related to outer retinal cellular structure and the functional properties of RGCs, which convey retinal output to the central visual system. The principal findings are as follows. (i) *Rs1* expression is restricted to photoreceptors and a very small number of RGCs. (ii) Each *Rs1* mutant develops a strong disease phenotype with an early onset that impacts all cells of the outer retina. (iii) RS1 distribution and disease severity varies across the panel of *Rs1* mutants. (iv) Female heterozygotes do not display a disease phenotype. (v) The electrophysiological output of the retina is compromised by synaptic remodeling of retinal circuits and by reduced signal-to-noise properties.

Cellular expression of *Rs1*

Prior studies of the mouse retina have found that *Rs1* is expressed in multiple retinal cell types during development (15). Specifically, Takada and co-workers (15) noted that a substantial fraction of RGCs are RS1-positive by immunohistochemistry as early as P1, and that RS1-positive RGCs and amacrine cells

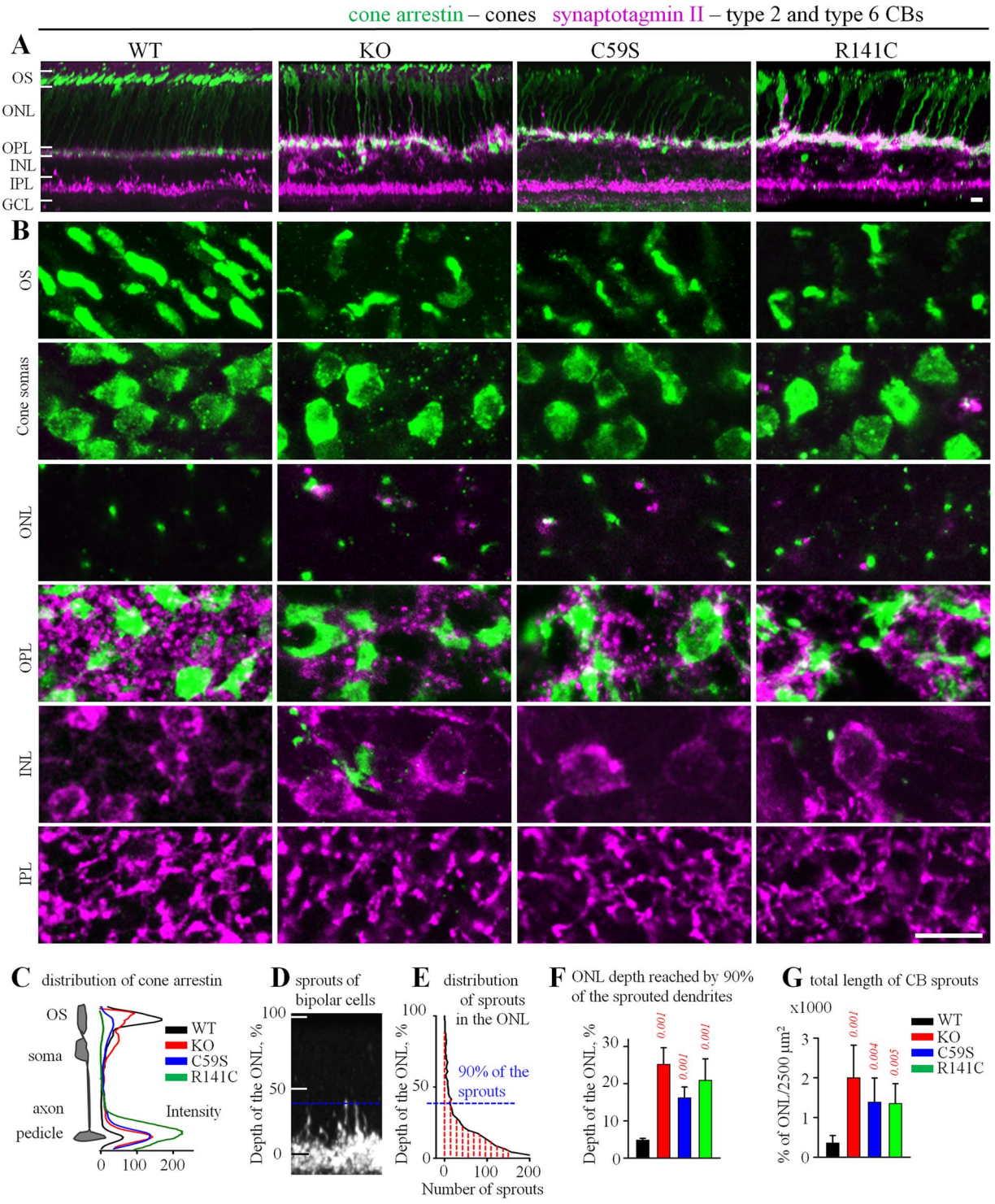

Figure 10. Morphological changes of cones and sprouting of cone BCs. (**A**) Vertical views reconstructed from confocal z-stack images of the retina whole-mounts. Cone arrestin (green) was concentrated in the OS of WT and was redistributed through the entire cone cell body in *Rs1* mutants. (**B**) Horizontal confocal sections from (A) demonstrate shortened cone OSs and malformation of cone axon terminals. Cone BCs labeled for synaptotagmin II (magenta) exhibited sprouting dendrites in the ONL. (**C**) Cone arrestin was redistributed in *Rs1* mutants as shown by the averaged fluorescent intensity profile. (**D**) A vertical view of a 250 µm^2 z-stack through the ONL rotated 90° and collapsed onto a single plane. Blue line marks the ONL position reached by 90% of sprouts. ONL was defined between the OPL (0%) and IS (100%). (**E**) Distribution of sprouts in the OPL from (D). Area under the curve represents total length of sprouts measured as a percentage of the ONL. (**F**) In all *Rs1* mutants, cone BC sprouts reached far into the IPL. The numbers represent depth of the ONL reached by 90% sprouts, as shown by the blue line in (D). (**G**) KO mice had greater total length of cone BC sprouts than C59S or R141C mice. The numbers indicate the area under curve in (E), marked by red vertical dashed lines. Bars indicate average (±SD) for 5–6 mice. Red *P*-values indicate significant difference from WT. Scale bar in (A) indicates 10 µm. OS: outer segment; ONL: outer nuclear layer; OPL: outer plexiform layer; INL: inner nuclear layer; IPL: inner plexiform layer and GCL: ganglion cell layer.

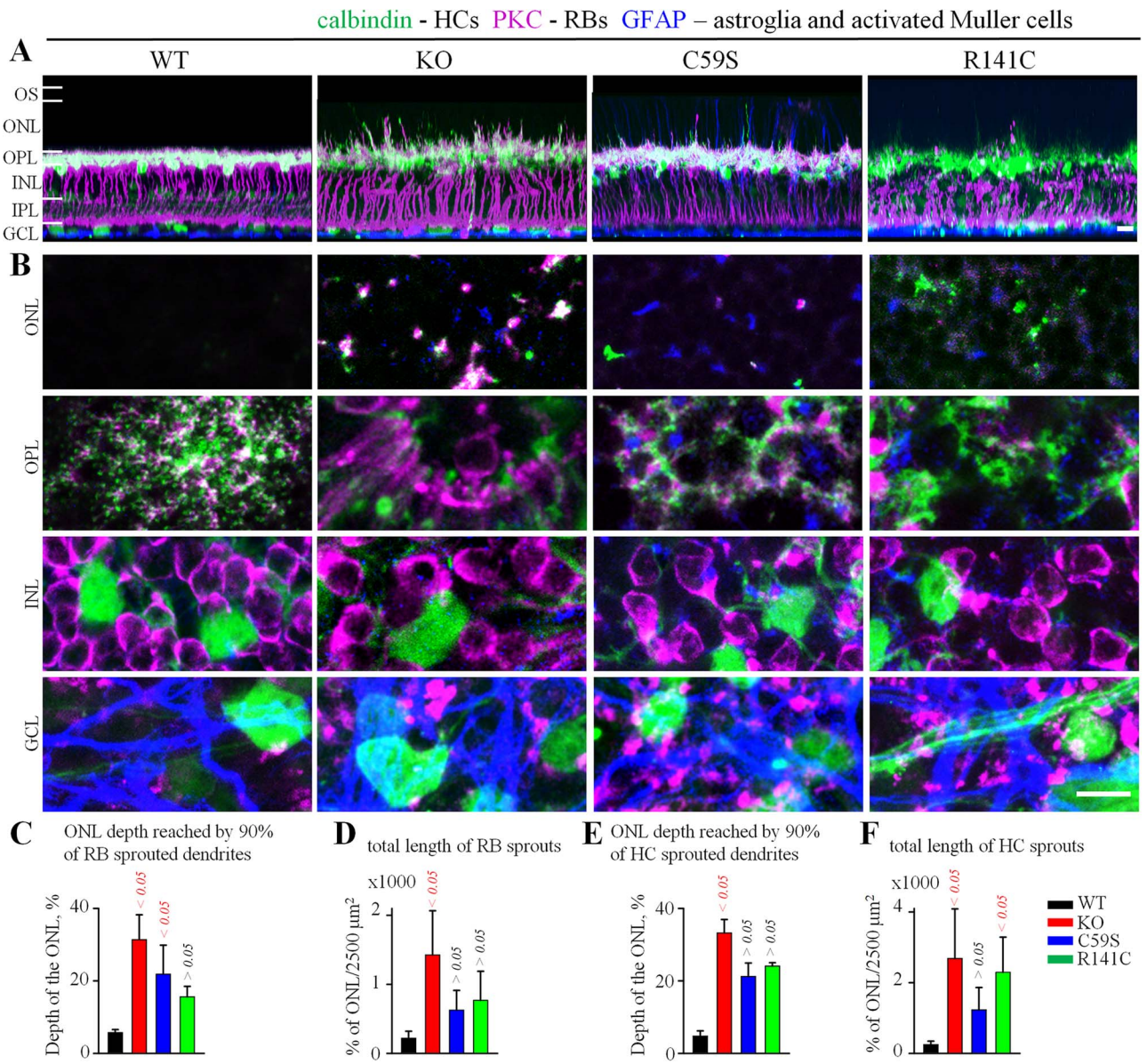

Figure 11. Morphological changes of rod BCs and HCs. (**A**) Vertical views reconstructed from confocal z-stacks of retinal whole mounts reveal sprouting of rod BCs (magenta) and HCs (green). (**B**) Horizontal confocal planes from (A). Rod BC and HC processes extend together into the ONL. Rod BCs and HCs had malformed and displaced somas. In *Rs1* mutants, astrocytes (blue) had dense processes and Müller cells (blue) expressed high levels of GFAP through the entire cell. (**C–F**) Quantification of rod BC and HC processes revealed prominent sprouting in all *Rs1* mutants, with the greatest amount seen in the KO. Bar indicates average (±SD) of 5–6 mice. Red P-values indicate significant difference from WT. Scale bar in (A) indicates 10 µm. OS: outer segment; ONL: outer nuclear layer; OPL: outer plexiform layer; INL: inner nuclear layer; IPL: inner plexiform layer; GCL: ganglion cell layer and PKC: protein kinase C.

were seen at P7, an age at which RS1-positive BCs were also documented. At later ages, RS1 labeled fewer cells in the inner retina and became primarily localized to photoreceptors. In this study, we labeled for the β-galactosidase protein encoded by *LacZ* knocked into the *Rs1* locus and for *Rs1* mRNA by RNAScope®. Outside of photoreceptors, we saw evidence for minimal *Rs1* expression only in a very small fraction of RGCs and only at early ages (Fig. 1). These results suggest that the retinal distribution of RS1 is more restricted than previously appreciated. This may be related to a different sensitivity and specificity of immunohistochemistry, RNAScope® and/or X-gal labeling.

RS1 is made and secreted by photoreceptors, but is found in all layers of the retina (Fig. 2A). This has been attributed to binding of secreted RS1 to extracellular sites on other retinal cells (45). Molecular *in vitro* studies of disease-causing *Rs1* mutations (1,23,46) have indicated that the R141C mutant protein is retained intracellularly, while the C59S variant is secreted not as a fully assembled octamer, but instead as a dimer. The IHC pattern observed in the mutant mice is consistent with this: RS1 immunostaining is present in the photoreceptor inner segments of C59S and R141C animals, as is β-galactosidase, a non-secreted marker protein, in the KO animals (cf. Fig. 1C–E with Fig. 2C and D), but the staining is mostly absent from all other retinal layers. We have no data concerning the secretion of RS1 variants *in vivo*, but we conjecture that if the C59S variant is secreted, it does not accumulate extracellularly.

Early onset disease phenotype

A severe disease phenotype was encountered at very early ages in all three *Rs1* mutant mouse models. Based on measures of schisis and retinal thickness, the most severe structural abnormalities were seen by SD-OCT at the earliest age examined (P15) for KO and at P18 for C59S and R141C mice. Disease severity then declined at older ages. ERG studies conducted in parallel revealed a similarly strong disease phenotype at the youngest ages examined.

We also examined these *Rs1* mutants at the cellular level. Cone photoreceptors displayed marked abnormalities at P21, including shortened, fewer and disorganized OS as well as malformed cone pedicles in which cone arrestin was present in much greater abundance as compared to the low levels seen in WT retina. Second order neurons were also abnormal. Enlarged somas were seen in cone BCs, rod BCs and also in HCs. In addition, each of these second order neurons extended ectopic processes neurites past the OPL and into the ONL. Ectopic projections have been previously reported in an *Rs1* KO (39) and are reminiscent of those observed in mouse models with abnormal control of glutamate release at the cone terminal, due to the absence of *Cacna1f* (41,42) or *Cabp4* (40). *Cacna1f* and *Cabp4* mutants have an ERG phenotype which resembles that of *Rs1* mutants in exhibiting a greater reduction of the b-wave as compared to the a-wave, suggesting that RS1 somehow contributes to the control of neurotransmitter release from photoreceptor terminals and/or to the establishment of a functional synapse. Consistent with these possibilities, RS1 has been reported to bind to CANCA1A subunits in the chick retina (47). Although we focused much of our effort on analysis of young retinas, moving to even younger ages will be required to determine which if any aspects of retinal development are ever normal in *Rs1* mutant mice.

The leading edge of the dark-adapted ERG a-wave reflects primarily the response of rod OS. This component was already abnormal at P15 and remained abnormal at later ages. These findings, along with the structural changes seen in cones, support the proposal (48) that *Rs1* mutations impact photoreceptor development. Another condition where photoreceptors are thought to not mature normally is retinopathy of prematurity (ROP; (49)). This conclusion is based on multiple lines of evidence, including analysis of rod photoreceptor function through the dark-adapted ERG a-wave (50), as well as psychophysical studies, which demonstrate that the spatial and temporal summation properties of patients with a history of ROP resemble those measured in normal subjects during ages when retinal development is incomplete (51,52). To test this idea further, it will be interesting to examine these visual properties in XLRS patients.

Genotype differences

While each *Rs1* mutant developed a severe disease phenotype, they were distinct across the three genotypes examined. The mildest disease phenotype was observed in the C59S mutant, which displayed a delayed peak of retinoschisis severity (Fig. 4B), and also retained larger amplitude ERGs at adult ages as compared to the KO or R141C model (Fig. 7). The C59S mutation is predicted to interfere with the ability of RS1-dimers to combine to form the mature octamer that is secreted. While little to no C59S RS1 is seen outside of photoreceptors by IHC (Fig. 2C), the milder phenotype seen in this model indicates that RS1-dimers may retain some function of WT RS1 for retinal development and/or maintenance. Perhaps there are intracellular functions for RS1 as well as extracellular ones, and the C59S dimer is capable of substituting for WT for some of these. Additionally, there may be physiological associations between C59S dimers similar to what has been described for subunits of intact dual-octamers of WT RS1, but they may be much weaker and unable to function fully as the 'bridging' structures proposed by Heymann and co-workers (53). In comparison to WT, the phenotype of the R141C model was more similar to the KO. Nevertheless, the early R141C phenotype was milder than the KO with respect to structural abnormalities (Fig. 4B), had peak schisis at a later age (Fig. 4B) and large ERG amplitudes in young mice (Fig. 7). Additional differences between the point mutants and KO were seen at the cellular level. For example, the KO displayed stronger sprouting of neurites by second-order neurons (Fig. 10C and D).

Rs1 mutant heterozygotes do not develop a disease phenotype

At the ERG and SD-OCT level, *Rs1* mutant heterozygous females (m/+) were as a group indistinguishable from WT littermates (+/+). This observation confirms that a single WT allele of *Rs1* expressed in approximately half of photoreceptors is sufficient to support normal retinal development and function, whether the corresponding mutant allele is null or a point mutation. These observations are consistent with the lack of phenotype in human female carriers. Interestingly, the retinal *Rs1* content of KO female heterozygotes (+/−) was comparable to that of WT homozygotes (Supplementary Material, Fig. S4). We cannot yet determine if this reflects a coordinated upregulation of RS1 production, a saturated capacity of the extracellular sites for RS1 binding, or some other mechanism. Although we examined only two human disease-causing mutations here (C59S, R141C), these were chosen to reflect two large general classes of disease mutations that impact formation of RS1 octamers (C59S) or that impede RS1 secretion (R141C). That a single WT allele expressed in approximately half of photoreceptors is sufficient for most aspects of normal retinal development and function supports efforts to use gene replacement therapy for XLRS (22). However, because of X-inactivation in females, each photoreceptor normally produces either WT RS1 or mutant RS1, but not both. The potential impact of co-expression of normal as well as mutant RS1 in the same photoreceptor remains to be determined, although this is the state induced by gene replacement therapy.

There may be some subtle differences in function for heterozygote human females, which we have not yet investigated in the mutant mice. Kim *et al.* (28) reported that some obligate XLRS carriers had localized retinal dysfunction on multifocal ERG testing, likely reflecting the stochastic process of X-chromosome inactivation. More recently, McAnany *et al.* (30) reported that standard flicker ERGs measured using standard protocols were not different between obligate XLRS carriers and controls, but did note abnormal timing of flicker ERGs recorded under conditions that may evoke destructive interference between rod and cone signals, reflecting a sub-clinical impact of the inactivation process.

Alterations in RGC electrophysiology

Our single-cell recordings from RGCs in *Rs1* mutant mice identified several abnormalities. These include observation of a large number of quiescent and non-responsive cells, suggesting a

mechanism for overall reduced visual activity in RS1. Furthermore, even in physiologically responsive cells, elevated background activity and as a direct result, decreased signal-to-noise properties would further exacerbate this deficit. These abnormalities were seen across both ON and OFF type RGCs, and were paralleled by significant structural changes within presynaptic ON and OFF BC circuits. Unlike what has been reported in models of glaucoma, where the disease process may directly affect RGCs and exhibited preferential vulnerability of OFF RGCs (54), the *Rs1* mutant phenotype is likely to reflect changes induced earlier in retinal signal processing and thus impact both ON and OFF circuitry. This is similar to earlier observations in models of retinitis pigmentosa (55). Together, these findings are consistent with the hypothesis that the elevated activity acts as a barrier for visual signal discrimination and raise the possibility that the reduced visual acuity and contrast sensitivity of XLRS patients (3) could reflect in part elevated intrinsic visual noise (56). Interestingly, for R141C mutants the RGC discrimination deficit was exacerbated by the decreased visual response indicating that the different *Rs1* mutations induce distinct pathophysiological changes.

Implications for XLRS

The results reported here from a panel of three *Rs1* mutants with disparate impacts on RS1 processing indicate that null and point mutations induce an early onset and severe disease phenotype, with older mice presenting later stages of a degenerative process. Further examination of the early disease stages will be needed to identify the ages at which treatment has the greatest potential to be effective and to determine the most relevant outcome measures. While yet to be examined, together these findings suggest the potential value of assessing visual impairment in XLRS patients using variations of standard clinical measures of visual function, such as letter charts with embedded noise (57,58).

Materials and Methods

Mice

Rs1 mutant mouse lines were generated for this study using Regeneron's VelociGene technology (59–62) as follows. An *Rs1* deficient line was created such that coding exons 1–3 were replaced with a lacZ reporter fused in-frame with the *Rs1* start (VelociGene allele identification number VG4333). In addition, two knock-in lines were generated carrying nucleotide 175T→A (missense mutation C59S) or 421C→T (missense mutation R141C), to mimic known human *RS1* mutations (1) (Supplementary Material, Fig. S5). The VelociGene® and VelociMouse® methods were then employed as described previously (59–62). Briefly, targeted ES cells (F1 hybrid 129S6SvEvTac/C57BL6NTac) identified by TaqMan assay and Sanger sequencing were injected into uncompacted eight-cell stage Swiss Webster embryos to produce healthy fully ES cell-derived mice. Male F0 mice were then crossed with C57Bl6/Ntac females to generate F1 heterozygotes. Subsequent mouse genotyping was done by Taqman assay and PCR using primers shown in Table 1.

LacZ expression

Mice were euthanized by CO_2 inhalation. Eyes were enucleated and fixed with 4% paraformaldehyde (PFA) in PBS (Electron Microscopy Sciences) for 3 h at 4°C. After three washings with 1× PBS (ThermoFisher Sci.), eyes were dissected under a dissecting microscope. The anterior portion and lens were removed; the rest of the eye (eyecup) was stained with HistoMark X-Gal Substrate Set (KPL) for 2 days at 37°C with gentle rotation. After staining, eyecups were rinsed with 1× PBS thoroughly, then were transferred to 30% sucrose overnight. The eyecups were embedded in Tissue-Tek® O.C.T. Compound (VWR) and frozen on dry ice. About 20-µm cryostat sections were prepared on Superfrost® Plus Micro Slides. Sections were dried for 30 min at room temperature, then washed three times with 1× PBS to remove O.C.T. Compound, and coverslipped with ProLong Gold Antifade Mountant with DAPI (ThermoFisher Sci.).

RNAScope®

The expression pattern of Rs1 mRNA in the engineered *Rs1* mouse lines was determined by *in situ* hybridization using RNAScope® according to manufacturer's specifications (Advanced Cell Diagnostics). Briefly, formalin or 4% PFA-fixed and paraffin or O.C.T. embedded mouse eye cups were cut into 5–10 µm sections and mounted on SUPERFROST® Plus glass slides. The procedure began with 10 min Pretreat 1 (ACD, 320037) at room temperature, followed by 20-min boiling in pretreat 2 (ACD, 320043) with Oster Steamer (IHC World, LLC, Model 5709) and pretreat 3 (ACD, 320037) for 30 min at 40°C in a HybEZ Oven (ACD, 310010). An additional DNase treatment step was included to reduce potential background from probe hybridization with chromosomal DNA. Slides were then washed three times with water, and a solution of DNase I (50 u/ml in 1× DNase I buffer, AM2224, Ambion) was added to the eye tissue for a 30-min incubation at 40°C. Slides were then washed five times with water, hybridized with RNAScope® probes for 2 h at 40°C and the remainder of the manufacturer's assay protocol was implemented (ACD, 322360) from amplified 1 to amplified 6. The slides were washed twice (2 min each at room temperature) with RNAScope® wash buffer (ACD, 310091). Signal was detected by incubation with red working solution (1:60 ratio of red B to red A) at room temperature for 10 min in the absence of light, followed by washing the slides in water several times and viewing under microscope. In some experiments, fluorescent signals were visualized and captured using an open-field Nikon Eclipse Ti-E microscope.

Cryostat sections and immunolabeling

Briefly, animals were euthanized by CO_2 inhalation. Eyes were enucleated and fixed with 4% PFA (Electron Microscopy Sciences) in 1× PBS (ThermoFisher) for 3 h at 4°C. After three washes with 1× PBS, eyes were dissected under a dissecting microscope. The anterior segment and lens were removed, and the rest of the eye (eyecup) was incubated in 30% sucrose at 4°C overnight. Eyecups were then embedded in TISSUE-TEK® O.C.T. Compound (VWR) and snap frozen on dry ice. About 10-µm cryostat sections were prepared on SUPERFROST® Plus Micro Slide used for immunofluorescent staining. Sections on slides were encircled with Liquid Blocker Super Pap Pen (Electron Microscopy Sciences) and air-dried 30 min at room temperature. Blocking solution was prepared as 5% normal goat serum (VectorLabs), 1% bovine serum albumin (Sigma-Aldrich) and 0.3% Triton-X 100 (Sigma-Aldrich) in 1× PBS. Wash solution was prepared as 0.1%

Table 1. Primer/probe sets for TAQMAN® assays

Name	Primer	Sequence (5′–3′)
Rs1-KOmTU	Forward	TGGGACAAGTGTAAATGAGGAC
	Reverse	AGTGGTGCTTGGCCTTATGC
	Probe	TCCCAGGCAAATCAGGACAAAGGGTC
Rs1-KOmTD	Forward	GAGCCAGCAACCTCACAC
	Reverse	GCATCCAGAGGAGCACAAGTC
	Probe	TGTAATGAACGGGTCTGACCTTTGCAA
Rs1-C59SmTU	Forward	TCGTGAAGGTCTTGATTTGATCCT
	Reverse	ACCTCCTGTCTCCACCTCTG
	Probe	AAGCACCATGTAAACTGGGCACCC
Rs1-C59SmTD	Forward	CCCTGGCTTGCCTGAGATG
	Reverse	GGACTTCCCTCACGCTGAGTT
	Probe	TCAGGTAAGACCCAATTGTCAATGCA
Rs1-R141CmTU	Forward	GAGTCGGGCTATGTCTGAAGG
	Reverse	GCCAACAGGTGCTGAGTTT
	Probe	CCAGATTTGGGATGATACCTCTTGATGC
Rs1-R141CmTD	Forward	CCTCTACATGCTGGGTCATCTG
	Reverse	GACCCACATTCATTTACAAACTGC
	Probe	TGTTCCTTCTCCACTGTACAAGCTCTC

Tween 20 (Amresco) in 1× PBS. Slides were placed in a staining container with black lid, washed three times with 1× PBS to remove O.C.T. Compound. Blocking solution was added to slides and remained for 1 h at room temperature. After removal of blocking solution, primary antibodies were diluted in blocking solution and applied to sections overnight at 4°C. On the second day, slides were washed three times with wash solution. Fluorophore-conjugated secondary antibodies were diluted at 1:1000 in 1× PBS and applied on sections for 1 h at room temperature (in the dark to avoid photobleaching). Slides were washed three times with 1× PBS and coverslipped with ProLong Gold Antifade Mountant with DAPI (ThermoFisher).

Antibodies and other reagents

Antibodies used in this study were goat anti-mouse albumin (Bethyl, A90-234A, 1:800, RRID:AB_67122); rabbit anti-cone arrestin (Millipore, AB15282, 1:10 000, RRID:AB_1163387), mouse anti-RS1 (63); mouse anti-RS1 (Novus, H00006247-B01P, 1:1000, RRID:AB_2180778); rabbit anti-calbindin (Swant, CB 38, 1:4000, RRID:AB_10000340), mouse anti-synaptotagmin II (Zebrafish International Resource Center, znp1, 1:2000, RRID:AB_10013783); mouse anti-PKC (SantaCruz, sc-8393, 1:8000, RRID:AB_628142), rabbit anti-Iba1 (Wako, 019–19741, 1:8000, RRID:AB_839504), chicken anti-GFAP (Chemicon, AB5541, 1:3000, RRID:AB_177521), ToPro for nuclear labeling (Invitrogen, T3605, 1:3000). Secondary antibodies were conjugated to Alexa 488 (1:1000; green fluorescence, Molecular Probes), Alexa 568 (1:1000; red fluorescence, Molecular Probes), Alexa 647 (1:400; far red fluorescence, Molecular probes) or Cy5 (1:500; far red fluorescence, Jackson ImmunoResearch).

Whole-mount immunolabeling

After euthanasia, eyes were removed and placed in oxygenized HEPES-buffered extracellular Ringer's solution, containing the following (in mM): NaCl (137), KCl (2.5), $CaCl_2$ (2.5), $MgCl_2$ (1.0), Na-HEPES (10), glucose (28), pH 7.4. The cornea was removed by an encircling cut above *ora serrata*, and the iris, lens and vitreous were extracted. The remaining eyecup, with the retina still attached to the retinal pigment epithelium, was submersion-fixed on a shaker in freshly prepared 4% PFA in 0.1 M phosphate saline (PBS, pH = 7.3) for 15 min at room temperature. After fixation, the eye cups were washed in PBS for 2 h and the retina was isolated from the eyecup. Retinal whole-mount preparations were blocked for 10 h in a PBS solution containing 5% chemiblocker (membrane-blocking agent, Chemicon), 0.5% Triton X-100 and 0.05% sodium azide (Sigma). Primary antibodies were diluted in the same solution and applied for 72 h, followed by incubation for 48 h in the appropriate secondary antibody. In multi-labeling experiments, eyecup preparations were incubated in a mixture of primary antibodies, followed by a mixture of secondary antibodies. All steps were completed at room temperature. After staining, the tissue was flat-mounted on a slide, and coverslipped using Vectashield mounting medium (H-1000, Vector Laboratories). The coverslip was sealed in place with nail polish. To avoid extensive squeezing and damage to the retina, small pieces of a broken glass cover slip (number 1 size) were placed in the space between the slide and the coverslip.

Electrophysiology

Extracellular spiking activity was obtained from RGCs in whole-mount retina in a loose-patch mode as described earlier (64), using electrodes filled with HEPES-buffered extracellular Ringer's solution. Electrodes were pulled from borosilicate glass (1B150F-4; WPI) with a P-97 Flaming/Brown puller (Sutter Instruments) and had a measured resistance of ∼4–7 MΩ. All recordings were made with a MultiClamp 700B patch-clamp amplifier (molecular devices) using signal 2 software (CED). Data were filtered at 5 kHz with a four-pole Bessel filter and were sampled at 15 kHz. After recordings, the cellular membrane under the pipette was ruptured to allow recordings of excitatory and inhibitory inputs by holding cells at the corresponding reversal potentials for Cl- and cation currents. To compare RGCs of similar classes, α-like RGCs were targeted based on large soma size and number of primary dendritic processes. To further confirm identity of the recorded cells, their morphology was examined after infusion of 100 µM AlexaFluor-568 hydrazide from the pipette solution. Contrast and fluorescent images of

the cell were documented with a digital camera attached to the microscope (Sony a7S). Dendritic stratification was measured relative to the proximal (0%) to the distal margins (100%) of the IPL from a confocal z-stack reconstruction of the RGC dendritic tree (Nikon C1). In general, ON cells were defined as stratifying at <60%, with OFF cells stratifying at >60% of IPL depth. The microscope's illuminator was used to deliver a 200 µm spot of light centered on the RGC. An aperture, a series of neutral density filters, the FN-C LWD condenser (Nikon) and a Uniblitz shutter (Vincent Associates, Rochester, NY) were used to control the size, intensity, focal plane and duration of the stimulus, respectively. Stimulation routines were controlled by signal 2 software (CED). The whole-mount retina was light adapted at 30 cd/m^2. To generate an intensity-response function, RGCs were presented with a 1 s stimulus separated by 10 s blank trials while maintaining the background light level throughout (65). The intensity of the light stimulus was changed in steps of either 0.25 or 0.5 log units, ranging from 10 to 10 000 Rh*/rod/s above adapting level, covering both mesopic and photopic conditions (66).

To measure how aberrant synaptic input interferes with responses, the SNR was calculated from spiking responses using Weber's equation: $SNR = (R - B)/B$, where R is the number of APs during a 1 s long light visual stimulus, and B is an AP count within a 1 s window preceding light stimulation.

Western blot

Total retinal protein (10–50 µg) was loaded onto 4–12% bis-tris gels in sample buffer (Nupage LDS sample buffer, Thermo) containing 4% SDS for protein separation and then transferred to nitrocellulose membrane (0.45 µm pore size, Invitrogen) followed by blocking with SuperBlock T20 (TBS, Thermo) for 1 h at room temperature. Blots were incubated with anti-RS1 antibody (Novus Biologicals USA, 1:4000) for 2 h at room temperature or overnight at 4°C. After incubation with anti-RS1 antibody, HRP conjugated anti-mouse polyclonal antibody (Cell Signaling) was added at 1:5000 for 1 h at room temperature. Protein bands were visualized and imaged using SuperSignal West Pico chemiluminescence (Thermo) by C-Digit Blot Scanner (Li-Cor).

ELISA

Mouse retina was isolated under dissection microscope and homogenized in 100 µl RIPA buffer per retina with protease inhibitor (Thermo Scientific™ Halt™ Protease Inhibitor Cocktails) in metal bead tube with Omini Homogenizer. Protein concentration was determined with BCA kit and then stored at −80°C until used for ELISA or Western blot. ELISA plates (NUNC) were coated with RS1 standard protein (Novus Biologicals, 0–40 ng/ml) and total retinal protein sample (1:2000 dilution in PBS) in triplicate at 4°C overnight. After three washes with T-TBS solution (T-TBS buffer, 0.05% Tween20 in TBS solution), plates were blocked with blocking buffer (1% BSA, 5% goat serum in TBS) for 1 h at room temperature. After three washes, anti-RS1 polyclonal antibody (Novus Biologicals USA, 1:4000 in blocking buffer) was added to the plates and incubated for 2 h at room temperature followed by addition of biotin-conjugated goat anti-mouse antibody (Jackson Lab, 1:5000) and Strepavidin-HRP (Thermo, 1:200), and, finally the substrate working solution (R&D systems) in the absence of light. The reaction was stopped by 2 N HCl. Optical density was recorded with SpectraMax Plus system (molecular devices).

Spectral-domain optical coherence tomography

Imaging procedures have been described in detail (67,68). Mice were anesthetized (sodium pentobarbital, 68 mg/kg) and pupils dilated with 1 µl eyedrops comprised of 0.5% tropicamide and 0.5% phenylephrine HCl. The corneal surface was anesthetized with a single application of ~10 µl of 0.5% proparacaine. SD-OCT images of the retina were collected along the horizontal and vertical meridians centered on the optic disk. Each set of orthogonal radial scans (1000 A-scans per B-scan by 10–15 frames) was converted to AVI files and exported to ImageJ with an axial scale of 1 µm/pixel. In ImageJ, each set of B-scans was co-registered and averaged using StackReg/TurboReg plug-ins (69). The field of view for each image was 0.464 mm (depth) by ~1.4 mm (width).

The area of schisis was measured from along the horizontal meridian by outlining the inner retina in ImageJ. ONL thickness was measured halfway from the optic disk to the edge of the image using the straight line tool. ONL thickness from the temporal and nasal regions was averaged to obtain a mean for each eye.

SD-OCT images were obtained from both eyes in the nasal and temporal cardinal directions from the optic nerve head (ONH). Each image was analyzed with respect to full retinal thickness, area of INL + OPL, and outer retinal thickness, as diagrammed in Figure 4. Full retinal thickness was measured from the vitreal surface to the choriocapillaris at distances of 260, 495 and 730 µm from the optic nerve for each image. These measurements were averaged within each mouse. The area of the INL + OPL was measured by tracing the relevant layers from the optic nerve to 645 µm. Nasal and temporal measurements were averaged within each mouse. Outer retinal thickness was measured as the area within each image that spanned the inner edge of the ONL and the tips of the OS. Nasal and temporal measurements were averaged within each mouse.

Electroretinography

WT and *Rs1* mutant mice were tested at ages ranging from 15 days to 28 weeks. Before the ERG analysis, mice were dark-adapted overnight in a temperature- and humidity-monitored cabinet and then were anesthetized with ketamine/xylazine (80/16 mg/kg) diluted in 0.9% saline. The pupils were dilated with eyedrops (1% tropicamide, 2.5% phenylephrine HCl and 1% cyclopentolate) and the corneal surface was anesthetized with 1% proparacaine HCl. ERGs were obtained from the corneal surface using a thin stainless-steel wire that was coiled at the end and wetted with a small drop of 1% carboxymethylcellulose. The active lead was referenced to a needle electrode placed in the cheek; a second needle electrode placed in the tail served as the ground lead. Flash stimuli were presented in an LKC (Gaithersburg, MD) ganzfeld, first to the dark-adapted eye (−3.6 to 2.1 log cd s/m^2) and then superimposed upon a steady 20 cd/m^2 background field following a 5-min light adaptation period (−0.8 to 2.1 log cd s/m^2). ERGs were amplified (0.03–1000 Hz), averaged and then stored using an LKC UTAS E-3000 signal averaging system.

The amplitude of the a-wave was measured at 8 ms after flash onset from the pre-stimulus baseline. The leading edge of the a-wave to a 1.4 log cd s/m^2 flash was measured using the equation:

$$P3(i,t) = \left(1 - \exp\left(-iA(t - td)^2\right)\right) R_{mP3} \quad (1)$$

where R_{mP3} is the maximum response amplitude, *A* is a measure of sensitivity and *td* is the delay in phototransduction (26).

The amplitude of the b-wave was measured from the a-wave trough to the b-wave peak. The function related b-wave amplitude to flash luminance has two limbs (70). We fit the first limb of this function using the Naka–Rushton equation (27):

$$R/R_{max} = L/(L + K) \quad (2)$$

where *R* is the amplitude of the a- or b-wave; R_{max} is the maximum amplitude of the a- or b-wave; *L* is the flash energy (log cd s/m^2) and *K* is the flash energy that elicits an amplitude of half R_{max} (half-saturation coefficient).

Data analysis

Statistical analysis was performed in either SPSS v. 22 (IBM, RRID:SCR_003210) or SigmaPlot v.11 (Systat, RRID:SCR_003210). For multiple comparisons, analysis of variance (ANOVA) with *post hoc* Tukey's test were used. Multiple samples from individual animals were averaged within subject, after which the data between animals were compared.

Supplementary Material

Supplementary material is available at *HMG* online.

Conflict of Interest statement

Yang Liu, Duo Sun, Hong Li, Tara Liao, Jingtai Cao, Yajun Tang, Susannah Brydges and Carmelo Romano are employees of Regeneron Pharmaceuticals.

Acknowledgements

We are grateful to Jason McAnany for comments on the manuscript. N.S.P. is a VA Research Career Scientist.

Funding

This work was supported by grants from the National Institutes of Health [R01 EY029796 to N.S.P. & B.T.S.; R01 EY026576 to B.T.S.; P30 EY025585]; by Research to Prevent Blindness; and by Regeneron Pharmaceuticals.

References

1. Molday, R.S., Kellner, U. and Weber, B.H.F. (2012) X-linked juvenile retinoschisis: clinical diagnosis, genetic analysis, and molecular mechanisms. *Progr. Ret. Eye Res.*, **31**(3), 195–212.
2. Forsius, H., Krause, U., Helve, J., Vuopala, V., Mustonen, E., Vainio-Mattila, B., Fellman, J. and Eriksson, A.W. (1973) Visual acuity in 183 cases of X-chromosomal retinoschisis. *Canad. J. Ophthalmol.*, **8**, 385–393.
3. Alexander, K.R., Barnes, C.S. and Fishman, G.A. (2005) Characteristics of contrast processing deficits in X-linked retinoschisis. *Vision Res.*, **45**(16), 2095–2107.
4. Tanino, T., Katsumi, O. and Hirose, T. (1985) Electrophysiological similarities between two eyes with X-linked recessive retinoschisis. *Doc. Ophth.*, **60**(2), 149–161.
5. Peachey, N.S., Fishman, G.A., Derlacki, D.J. and Brigell, M.G. (1987) Psychophysical and electroretinographic findings in X-linked juvenile retinoschisis. *Arch. Ophthalmol.*, **105**(4), 513–516.
6. Ali, A., Feroze, A.H., Rizvi, Z.H. and Rehman, T.U. (2003) Consanguineous marriage resulting in homozygous occurrence of X-linked retinoschisis in girls. *Amer. J. Ophthalmol.*, **136**(4), 767–769.
7. Rodríguez, F.J., Rodríguez, A., Mendoza-Londoño, R. and Tamayo, M.L. (2005) X-linked retinoschisis in three females from the same family: a phenotype-genotype correlation. *Retina*, **25**(1), 69–74.
8. Saleheen, D., Ali, A., Khanum, S., Ozair, M.Z., Zaidi, M., Sethi, M.J., Khan, N. and Frossard, P. (2008) Molecular analysis of the XLRS1 gene in 4 females affected with X-linked juvenile retinoschisis. *Canad. J. Ophthalmol.*, **43**(5), 596–599.
9. Staffieri, S.E., Rose, L., Chang, A., De Roach, J.N., McLaren, T.L., Mackey, D.A., Hewitt, A.W. and Lamey, T.M. (2015) Clinical and molecular characterization of females affected by X-linked retinoschisis. *Clin. Exp. Ophthalmol.*, **43**(7), 643–647.
10. Sauer, C.G., Gehrig, A., Warneke-Wittstock, R., Marquardt, A., Ewing, C.C., Gibson, A., Lorenz, B., Jurklies, B. and Weber, B.H. (1997) Positional cloning of the gene associated with X-linked juvenile retinoschisis. *Nat. Genet.*, **17**(2), 164–170.
11. Eksandh, L.C., Ponjavic, V., Ayyagari, R., Bingham, E.L., Hiriyanna, K.T., Andreasson, S., Ehinger, B. and Sieving, P.A. (2000) Phenotypic expression of juvenile X-linked retinoschisis in Swedish families with different mutations in the XLRS1 gene. *Arch. Ophthalmol.*, **118**(8), 1098–1104.
12. Simonelli, F., Cennamo, G., Ziviello, C., Testa, F., de Crecchio, G., Nesti, A., Manitto, M.P., Ciccodicola, A., Banfi, S., Brancato, R. *et al.* (2003) Clinical features of X linked juvenile retinoschisis associated with new mutations in the XLRS1 gene in Italian families. *Br. J. Ophthalmol.*, **87**(9), 1130–1134.
13. Sergeev, Y.V., Vitale, S., Sieving, P.A., Vincent, A., Robson, A.G., Moore, A.T., Webster, A.R. and Holder, G.E. (2013) Molecular modeling indicates distinct classes of missense variants with mild and severe XLRS phenotypes. *Hum. Mol. Genet.*, **22**(23), 4756–4767.
14. Bowles, K., Cukras, C., Turriff, A., Sergeev, Y., Vitale, S., Bush, R.A. and Sieving, P.A. (2011) X-linked retinoschisis: *RS1* mutation severity and age affect the ERG phenotype in a cohort of 68 affected male subjects. *Invest. Ophthalmol. Vis. Sci.*, **52**(12), 9250–9256.
15. Takada, Y., Fariss, R.N., Tanikawa, A., Zeng, Y., Carper, D., Bush, R. and Sieving, P.A. (2004) A retinal neuronal developmental wave of retinoschisin expression begins in ganglion cells during layer formation. *Invest. Ophthalmol. Vis. Sci.*, **45**(9), 3302–3312.
16. Tolun, G., Vijayasarathy, C., Huang, R., Zeng, Y., Li, Y., Steven, A.C., Sieving, P.A. and Heymann, J.B. (2016) Paired octamer rings of retinoschisin suggest a junctional model for cell-cell adhesion in the retina. *Proc. Natl. Acad. Sci. U.S.A.*, **113**(19), 5287–5292.
17. Weber, B.H., Schrewe, H., Molday, L.L., Gehrig, A., White, K.L., Seeliger, M.W., Jaissle, G.B., Friedburg, C., Tamm, E. and Molday, R.S. (2002) Inactivation of the murine X-linked juvenile retinoschisis gene, Rs1h, suggests a role of retinoschisin in retinal cell layer organization and synaptic structure. *Proc. Natl. Acad. Sci. U.S.A.*, **99**(9), 6222–6227.
18. Zeng, Y., Takada, Y., Kjellstrom, S., Hiriyanna, K., Tanikawa, A., Wawrousek, E., Smaoui, N., Caruso, R., Bush, R.A. and Sieving, P.A. (2004) RS-1 gene delivery to an adult Rs1h knockout mouse model restores ERG b-wave with reversal

of the electronegative waveform of X-linked retinoschisis. *Invest. Ophthalmol. Vis. Sci.*, **45**(9), 3279–3285.
19. Jablonski, M.M., Dalke, C., Wang, X., Lu, L., Manly, K.F., Pretsch, W., Favor, J., Pardue, M.T., Rinchik, E.M., Williams, R.W. *et al.* (2005) An ENU-induced mutation in *Rs1h* causes disruption of retinal structure and function. *Mol. Vision*, **11**, 569–581.
20. Chen, D., Xu, T., Tu, M., Xu, J., Zhou, C., Cheng, L., Yang, R., Yang, T., Zheng, W., He, X. *et al.* (2018) Recapitulating X-linked juvenile retinoschisis in mouse model by knock-in patient-specific novel mutation. *Front. Mol. Neurosci.*, **10**, 453.
21. Bush, R.A., Wei, L.L. and Sieving, P.A. (2015) Convergence of human genetics and animal studies: gene therapy for X-linked retinoschisis. *Cold Spring Harb. Persp. Med.*, **5**(8), a017368.
22. Cukras, C., Wiley, H.E., Jeffrey, B.G., Sen, H.N., Turriff, A., Zeng, Y., Vijayasarathy, C., Marangoni, D., Ziccardi, L., Kjellstrom, S. *et al.* (2018) Retinal AAV8-RS1 gene therapy for X-linked retinoschisis: initial findings from a phase I/IIa trial by intravitreal delivery. *Mol. Ther.*, **26**(9), 2282–2294.
23. Wu, W.W. and Molday, R.S. (2003) Defective discoidin domain structure, subunit assembly, and endoplasmic reticulum processing of retinoschisin are primary mechanisms responsible for X-linked retinoschisis. *J. Biol. Chem.*, **278**(30), 28139–28146.
24. Condon, G.P., Brownstein, S., Wang, N.-S., Kearns, A.F. and Ewing, C.C. (1986) Congenital hereditary (juvenile X-linked) retinoschisis. Histopathologic and ultrastructural findings in three eyes. *Arch. Ophthalmol.*, **104**, 576–583.
25. Gerth, C., Zawadzki, R.J., Werner, J.S. and Heon, E. (2008) Retinal morphological changes of patients with X-linked retinoschisis evaluated by Fourier-domain optical coherence tomography. *Arch. Ophthalmol.*, **126**(6), 807–811.
26. Breton, M.E., Schueller, A.W., Lamb, T.D. and Pugh, E.N., Jr. (1994) Analysis of ERG a-wave amplification and kinetics in terms of the G-protein cascade of phototransduction. *Invest. Ophthalmol. Vis. Sci.*, **35**(1), 295–309.
27. Fulton, A.B. and Rushton, W.A.H. (1978) The human rod ERG: correlation with psychophysical responses in light and dark adaptation. *Vision Res.*, **18**(7), 793–800.
28. Kim, L.S., Seiple, W., Fishman, G.A. and Szlyk, J.P. (2007) Multifocal ERG findings in carriers of X-linked retinoschisis. *Doc. Ophthalmol.*, **114**(1), 21–26.
29. Saldana, M., Thompson, J., Monk, E., Trump, D., Long, V. and Sheridan, E. (2007) X-linked retinoschisis in a female with a heterozygous RS1 missense mutation. *Amer. J. Med. Genet. A*, **143**, 608–609.
30. McAnany, J.J., Park, J.C., Collison, F.T., Fishman, G.A. and Stone, E.M. (2016) Abnormal 8-Hz flicker electroretinograms in carriers of X-linked retinoschisis. *Doc. Ophthalmol.*, **133**(1), 61–70.
31. Wässle, H. (2004) Parallel processing in the mammalian retina. *Nature Rev. Neurosci.*, **5**(10), 747–757.
32. Ou, J., Vijayasarathy, C., Ziccardi, L., Chen, S., Zeng, Y., Marangoni, D., Pope, J.G., Bush, R.A., Wu, Z., Li, W. and Sieving, P.A. (2015) Synaptic pathology and therapeutic repair in adult retinoschisis mouse by AAV-RS1 transfer. *J. Clin. Invest.*, **125**(7), 2891–2903.
33. Penn, R.D. and Hagins, W.A. (1969) Signal transmission along retinal rods and the origin of the electroretinographic a-wave. *Nature*, **223**(5202), 201–204.
34. Kofuji, P., Ceelen, P., Zahs, K.R., Surbeck, L.W., Lester, H.A. and Newman, E.A. (2000) Genetic inactivation of an inwardly rectifying potassium channel (Kir4.1 subunit) in mice: phenotypic impact in retina. *J. Neurosci.*, **20**(15), 5733–5740.
35. Sharma, S., Ball, S.L. and Peachey, N.S. (2005) Pharmacological studies of the mouse cone electroretinogram. *Vis. Neurosci.*, **22**(5), 631–636.
36. Zhu, X., Li, A., Brown, B., Weiss, E.R., Osawa, S. and Craft, C.M. (2002) Mouse cone arrestin expression pattern: light induced translocation in cone photoreceptors. *Mol. Vision*, **8**, 462–471.
37. Wässle, H., Puller, C., Muller, F. and Haverkamp, S. (2009) Cone contacts, mosaics, and territories of bipolar cells in the mouse retina. *J. Neurosci.*, **29**(1), 106–117.
38. Nikonov, S.S., Brown, B.M., Davis, J.A., Zuniga, F.I., Bragin, A., Pugh, E.N. and Craft, C.M. (2008) Mouse cones require an arrestin for normal inactivation of phototransduction. *Neuron*, **59**(3), 462–474.
39. Takada, Y., Vijayasarathy, C., Zeng, Y., Kjellstrom, S., Bush, R.A. and Sieving, P.A. (2008) Synaptic pathology in retinoschisis knockout ($Rs1^{-/y}$) mouse retina and modification by rAAV-Rs1 gene delivery. *Invest. Ophthalmol. Vis. Sci.*, **49**(8), 3677–3686.
40. Haeseleer, F., Imanishi, Y., Maeda, T., Possin, D.E., Maeda, A., Lee, A., Rieke, F. and Palczewski, K. (2004) Essential role of Ca^{2+}-binding protein 4, a Cav1.4 channel regulator, in photoreceptor synaptic function. *Nat. Neurosci.*, **7**(10), 1079–1087.
41. Mansergh, F., Orton, N.C., Vessey, J.P., Lalonde, M.R., Stell, W.K., Tremblay, F., Barnes, S., Rancourt, D.E. and Bech-Hansen, N.T. (2005) Mutation of the calcium channel gene *Cacna1f* disrupts calcium signaling, synaptic transmission and cellular organization in mouse retina. *Hum. Mol. Genet.*, **14**(20), 3035–3046.
42. Chang, B., Heckenlively, J.R., Bayley, P.R., Brecha, N.C., Davisson, M.T., Hawes, N.L., Hirano, A.A., Hurd, R.E., Ikeda, A., Johnson, B.A. *et al.* (2006) The *nob2* mouse, a null mutation in Cacna1f: anatomical and functional abnormalities in the outer retina and their consequences on ganglion cell visual responses. *Vis. Neurosci.*, **23**(1), 11–24.
43. Ekstrom, P., Sanyal, S., Narfstrom, K., Chader, G.J. and van Veen, T. (1988) Accumulation of glial fibrillary acidic protein in Muller radial glia during retinal degeneration. *Invest. Ophthalmol. Vis. Sci.*, **29**(9), 1363–1371.
44. Sarthy, P.V., Fu, M. and Huang, J. (1991) Developmental expression of the glial fibrillary acidic protein (GFAP) gene in the mouse retina. *Cell. Mol. Neurobiol.*, **11**(6), 623–637.
45. Reid, S.N.M., Yamashita, C. and Farber, D.B. (2003) Retinoschisin, a photoreceptor-secreted protein, and its interaction with bipolar and Müller cells. *J. Neurosci.*, **23**(14), 6030–6040.
46. Sun, D., Liu, Y., Zazzarino, N., Tao, J., Martin, J., Olson, W., Cao, J. and Romano, C. (2018) Wild type and mutant retinoschisin subunits co-assemble when expressed in the same cells. *Invest. Ophthalmol. Vis. Sci.*, **59**.
47. Shi, L., Jian, K., Ko, M.L., Trump, D. and Ko, G.Y. (2009) Retinoschisin, a new binding partner for L-type voltage-gated calcium channels in the retina. *J. Biol. Chem.*, **284**(6), 3966–3975.
48. Ziccardi, L., Vijayasarathy, C., Bush, R.A. and Sieving, P.A. (2012) Loss of retinoschisin (RS1) cell surface protein in maturing mouse rod photoreceptors elevates the luminance threshold for light-driven translocation of transducin but not arrestin. *J. Neurosci.*, **32**(38), 13010–13021.
49. Hansen, R.M., Moskowitz, A., Akula, J.D. and Fulton, A.B. (2017) The neural retina in retinopathy of prematurity. *Prog. Ret. Eye Res.*, **56**, 32–57.
50. Harris, M.E., Moskowitz, A., Fulton, A.B. and Hansen, R.M. (2011) Long-term effects of retinopathy of prematurity (ROP)

on rod and rod-driven function. *Doc. Ophthalmol.*, **122**(1), 19–27.
51. Hansen, R.M., Tavormina, J.L., Moskowitz, A. and Fulton, A.B. (2014) Effect of retinopathy of prematurity on scotopic spatial summation. *Invest. Ophthalmol. Vis. Sci.*, **55**(5), 3311–3313.
52. Hansen, R.M., Moskowitz, A., Tavormina, J.L., Bush, J.N., Soni, G. and Fulton, A.B. (2015) Temporal summation in children with a history of retinopathy of prematurity. *Invest. Ophthalmol. Vis. Sci.*, **56**(2), 914–917.
53. Heymann, J.B., Vijayasarathy, C., Huang, R.H., Dearborn, A.D., Sieving, P.A. and Steven, A.C. (2019) Cryo-EM of retinoschsin branched networks suggests an intercellular adhesive scaffold in the retina. *J. Cell Biol.*, **218**(3), 1027–1038.
54. Ou, Y., Jo, R.E., Ullian, E.M., Wong, R.O. and Della Santina, L. (2016) Selective vulnerability of specific retinal ganglion cell types and synapses after transient ocular hypertension. *J. Neurosci.*, **36**(35), 9240–9252.
55. Yee, C.W., Toychiev, A.H., Ivanova, E. and Sagdullaev, B.T. (2014) Aberrant synaptic input to retinal ganglion cells varies with morphology in a mouse model of retinal degeneration. *J. Comp. Neurol.*, **522**(18), 4085–4099.
56. Pelli, D. and Farell, B. (1999) Why use noise? *J. Opt. Soc. Amer., A: Opt. Image Sci. Vis.*, **16**(3), 647–653.
57. Pelli, D.G., Levi, D.M. and Chung, S.T. (2004) Using visual noise to characterize amblyopic letter identification. *J. Vision*, **4**, 904–920.
58. Pelli, D.G., Robson, J.G. and Wilkins, A.J. (1988) The design of a new letter chart for measuring contrast sensitivity. *Clin. Vision. Sci.*, **2**, 187–199.
59. Dechiara, T.M., Poueymirou, W.T., Auerbach, W., Frendewey, D., Yancopoulos, G.D. and Valenzuela, D.M. (2009) VelociMouse: fully ES cell-derived F0-generation mice obtained from the injection of ES cells into eight-cell-stage embryos. *Meth. Mol. Biol.*, **530**, 311–324.
60. DeChiara, T.M., Poueymirou, W.T., Auerbach, W., Frendewey, D., Yancopoulos, G.D. and Valenzuela, D.M. (2010) Producing fully ES cell-derived mice from eight-cell stage embryo injections. *Meth. Enzymol.*, **476**, 285–294.
61. Poueymirou, W.T., Auerbach, W., Frendewey, D., Hickey, J.F., Escaravage, J.M., Esau, L., Doré, A.T., Stevens, S., Adams, N.C., Dominguez, M.G. *et al.* (2007) F0 generation mice fully derived from gene-targeted embryonic stem cells allowing immediate phenotypic analyses. *Nat. Biotech.*, **25**(1), 91–99.
62. Valenzuela, D.M., Murphy, A.J., Frendewey, D., Gale, N.W., Economides, A.N., Auerbach, W., Poueymirou, W.T., Adams, N.C., Rojas, J., Yasenchak, J. *et al.* (2003) High-throughput engineering of the mouse genome coupled with high-resolution expression analysis. *Nat. Biotechnol.*, **21**(6), 652–659.
63. Molday, L.L., Hicks, D., Sauer, C.G., Weber, B.H.F. and Molday, R. (2001) Expression of X-linked retinoschisis protein rs1 in photoreceptors and bipolar cells. *Invest. Ophthalmol. Vis. Sci.*, **42**, 816–825.
64. Toychiev, A.H., Sagdullaev, B., Yee, C.W., Ivanova, E. and Sagdullaev, B.T. (2013) A time and cost efficient approach to functional and structural assessment of living neuronal tissue. *J. Neurosci. Meth.*, **214**, 105–112.
65. Toychiev, A.H., Ivanova, E., Yee, C.W. and Sagdullaev, B.T. (2013) Block of gap junctions eliminates aberrant activity and restores light responses during retinal degeneration. *J. Neurosci.*, **33**(35), 13972–13977.
66. Deans, M.R., Volgyi, B., Goodenough, D.A., Bloomfield, S.A. and Paul, D.L. (2002) Connexin36 is essential for transmission of rod-mediated visual signals in the mammalian retina. *Neuron*, **36**(4), 703–712.
67. Bell, B.A., Kaul, C., Bonilha, V.L., Rayborn, M.E., Shadrach, K. and Hollyfield, J.G. (2015) The BALB/c mouse: effect of standard vivarium lighting on retinal pathology during aging. *Exp. Eye Res.*, **135**, 192–205.
68. Bell, B.A., Kaul, C. and Hollyfield, J.G. (2014) A protective eye shield for prevention of media opacities during small animal ocular imaging. *Exp. Eye Res.*, **127**, 280–287.
69. Thevenaz, P., Ruttimann, U.E. and Unser, M. (1998) A pyramid approach to subpixel registration based on intensity. *IEEE Trans. Image Proc.*, **7**(1), 27–41.
70. Peachey, N.S., Alexander, K.R. and Fishman, G.A. (1987) The luminance-response function of the dark-adapted human electroretinogram. *Vision Res.*, **29**, 263–270.